nature communications

Article

https://doi.org/10.1038/s41467-025-67254-x

αPD-1-conjugated acid-cleavable nanodrugs overcomes cellular immunotherapy barriers in pancreatic tumors

Received: 8 April 2025

Accepted: 23 November 2025

Ziqi Gan[1,2,5], **Jing Huang**[1,3,4,5], **Shuting Duan**[1,5], **Minzhao Lin**[3], **Shaohui Deng**[3], **Sicong Huang**[3], **Jiachen Wang**[3], **Xintao Shuai**[1] **& Zecong Xiao**[1]

Overcoming barriers in solid tumor immunotherapy remains challenging, with adoptive T cell therapies limited by antigen loss, poor tumor infiltration, and T cell exhaustion. Here, we present a nanoengineered tumor-infiltrating lymphocyte (TIL) therapy using anti-PD-1 antibody (αPD-1)-conjugated ZIF-8 nanoparticles to effectively suppress pancreatic tumor growth. These nanoparticles release hyaluronidase (HAase) and decitabine (DEC) in acidic tumor microenvironments, promoting stroma degradation and C−C motif chemokine ligand 5 (CCL5) secretion, while retaining αPD-1 on TILs to prevent exhaustion. CCL5 recruits additional nanodrug-loaded TILs for further release of HAase and DEC, establishing a self-reinforcing infiltration loop. This approach increases TIL infiltration by 12-fold in immunodeficient mice and, in immunocompetent settings, mobilizes both exogenous TILs and endogenous $CD8^+$ T cells, enabling tumor eradication and metastasis suppression with 10-fold lower TIL doses than conventional therapies. Collectively, this nanoengineered TIL therapy offers a potential strategy for addressing immune-resistant tumors, showing distinct benefits in stromal-rich settings.

The advent of adoptive cell transfer (ACT) therapies, particularly chimeric antigen receptor T-cell (CAR-T) therapy, has revolutionized cancer treatment[1]. Despite notable success in hematologic malignancies, the therapeutic efficacy of CAR-T and other genetically modified cell-based immunotherapies in solid tumors remains suboptimal due to the biological complexities inherent in solid tumors[2]. A major limitation is their reliance on antigen-specific targeting, which is susceptible to tumor heterogeneity and antigen loss, leading to tumor escape and treatment failure[3]. TIL therapy offers a promising alternative. Unlike therapies targeting one or two antigens, TILs naturally possess polyclonal T-cell receptor (TCR) repertoires that recognize a broad spectrum of tumor-specific epitopes, minimizing antigen escape[4]. Additionally, TILs exhibit intrinsic tumor tropism, improving their homing to tumor niches compared to peripherally activated T cells[5,6]. These attributes, coupled with their favorable safety profile relative to genetically modified cell products, position TIL therapy as a compelling alternative for solid tumors.

However, the efficacy of TIL therapy in immune-resistant solid tumors is constrained by microenvironmental barriers. Pancreatic ductal adenocarcinoma (PDAC), a prototypical immunogenically “cold” malignancy, exemplifies this challenge: dense desmoplastic stroma and aberrant chemokine gradients exclude immune cells from tumor cores, hindering therapeutic outcomes[7]. Beyond stromal exclusion, adoptive T cells in PDAC often undergo dysfunction and exhaustion due to repeated TCR stimulation and harsh tumor microenvironment (TME) conditions, including hypoxia, acidosis, and immunosuppressive signals[8]. These stressors induce the upregulation of inhibitory immune checkpoints (e.g., PD-1, CTLA-4,

---

[1]Nanomedicine Research Center, The Third Affiliated Hospital of Sun Yat-sen University, Guangzhou, PR China. [2]Houston Methodist Neal Cancer Center, Houston Methodist Research Institute, Houston, TX, USA. [3]PCFM Lab of Ministry of Education, School of Materials Science and Engineering, Sun Yat-sen University, Guangzhou, PR China. [4]School of Biomedical Engineering and Informatics, Nanjing Medical University, Nanjing, PR China. [5]These authors contributed equally: Ziqi Gan, Jing Huang, Shuting Duan. e-mail: zgan@houstonmethodist.org; shuaixt@mail.sysu.edu.cn; xiaozc5@mail.sysu.edu.cn

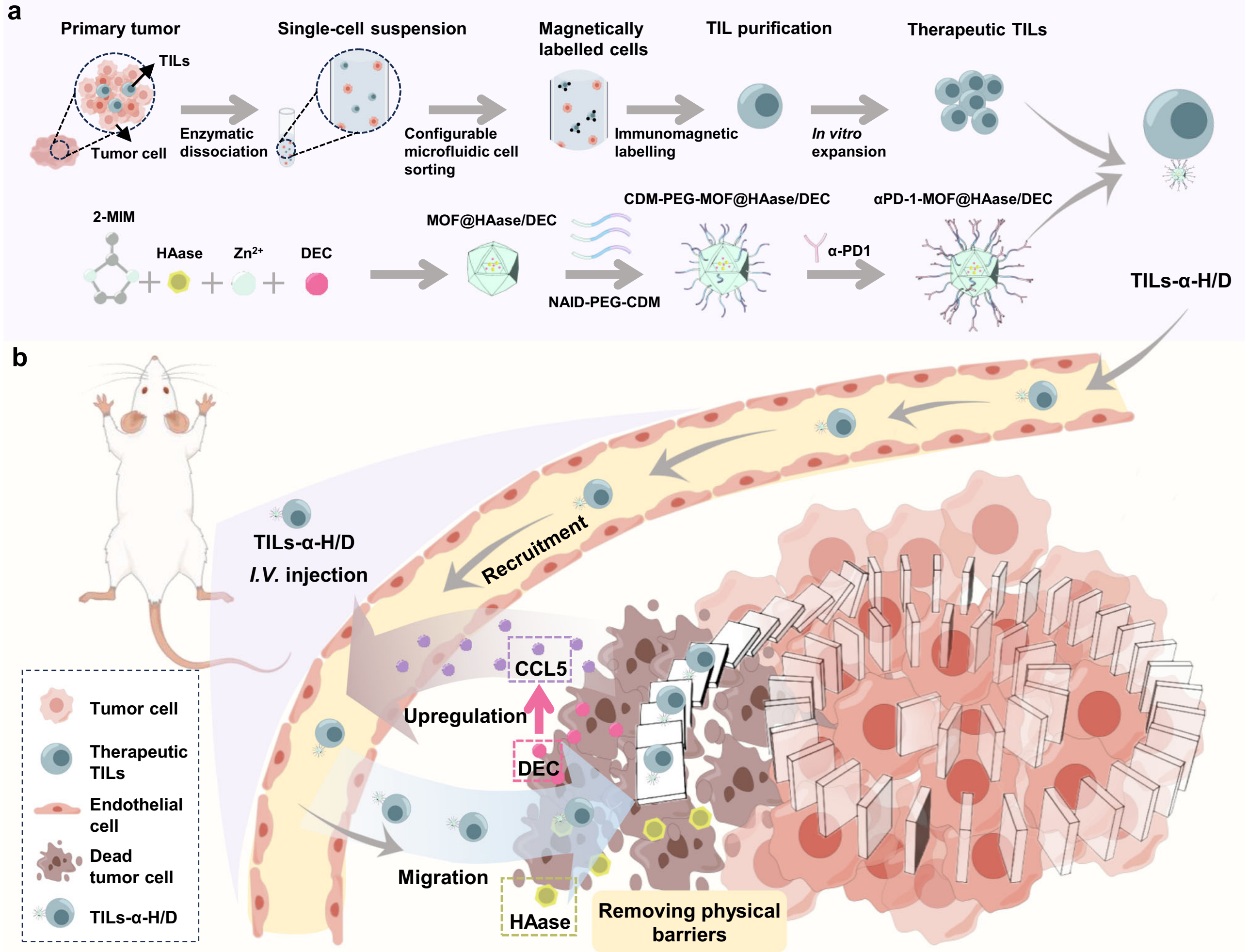

Fig. 1 | Schematic illustration of the preparation of nanodrug-carrying TILs (TILs-α-H/D) and their antitumor effect. a The preparation process of TILs and the nanodrug α-H/D, including the synthesis of TILs-α-H/D. **b** The antitumor mechanism of TILs-α-H/D, wherein TILs utilize their natural tumor-homing properties to deliver the nanodrug into the tumor. Upon reaching the tumor microenvironment, the nanodrug releases HAase, which degrades hyaluronic acid, facilitating TILs infiltration into the tumor. Simultaneously, DEC upregulates CCL5 expression within the tumor, further enhancing the recruitment of TILs-α-H/D into the tumor. TILs tumor-infiltrating lymphocytes; HAase hyaluronidase; DEC decitabine; NAID-PEG-CDM 1-(3-aminopropyl)imidazole)-(polyethylene glycol)-(2,5-Dihydro-4-methyl-2,5-dioxo-3-furanpropanoic acid); α-PD-1 anti-PD-1 antibody; MOF metal–organic framework; CCL5 chemokine (C–C motif) ligand 5; α-H/D αPD-1-MOF@HAase/DEC; TILs-α-H/D TILs-αPD-1-MOF@HAase/DEC.

and LAG-3), ultimately curtailing T cell persistence and cytotoxic efficacy post-infusion[9]. Thus, overcoming stromal and exhaustion barriers is crucial to unlocking the full potential of TIL therapy in PDAC and other immune-resistant tumors, where conventional single-agent immunotherapies, including checkpoint blockade (ICB), have so far failed to achieve meaningful efficacy[10].

To address these challenges, we explored nanotechnology to enhance TIL's antitumor capabilities by engineering multifunctional nanoparticle (NP) conjugates. Our prior work[11,12] has shown that well-designed NPs can "hitchhike" on circulating T cells, delivering immunomodulatory payloads directly to tumors without compromising T-cell function. These NPs can actively concentrate in tumor sites along with the circulating T cells, and once arriving, the NPs-T cell complexes will locally release therapeutic payloads either in a pseudo-autocrine fashion to support T cell survival, proliferation, and effector functions, or in a pseudo-paracrine manner, reshaping the surrounding immunosuppressive TME or activating bystander immune cells[13,14]. Building upon this platform, we reasoned that equipping TILs with such backpacking NPs could enhance their antitumor activity and potentially overcome current ACT barriers in immune-resistant solid tumors, leveraging TILs' natural tumor-homing and broad antigen recognition capabilities.

In this work, we use pancreatic cancer as a model to explore the potential of nanoengineered TIL therapy (Fig. 1). We employ an acid-sensitive ZIF-8 metal–organic framework (MOF) nanocarrier to encapsulate HAase and DEC, which degrades the tumor matrix and enhances TIL infiltration, αPD-1 is tethered to the nanoparticles, enabling them to bind to TILs and prevent exhaustion. After reinfusion, these nanodrug-carrying TILs navigate to tumor foci, where the acidic TME triggers MOF disintegration, releasing the payloads. HAase degrades the dense stroma, facilitating TIL infiltration and DEC penetration, which reactivates CCL5 production and further recruits TILs. This system may establish a self-amplifying loop of TIL recruitment, enhancing antitumor efficacy in immunologically "cold" tumor types.

Results

Polymer synthesis and nanodrug preparation

The synthesis of 1-(3-aminopropyl)imidazole)-(polyethylene glycol)-(2,5-Dihydro-4-methyl-2,5-dioxo-3-furanpropanoic acid (NAID-PEG-CDM) is shown in Supplementary Fig. 1 and its characterization was confirmed via ^{1}H NMR (Supplementary Figs. 2, 3 and Fig. 2a). The preparation of αPD-1-MOF@H/D is illustrated in Fig. 2b; briefly, an aqueous solution containing HAase, polyvinyl pyrrolidone (PVP) and

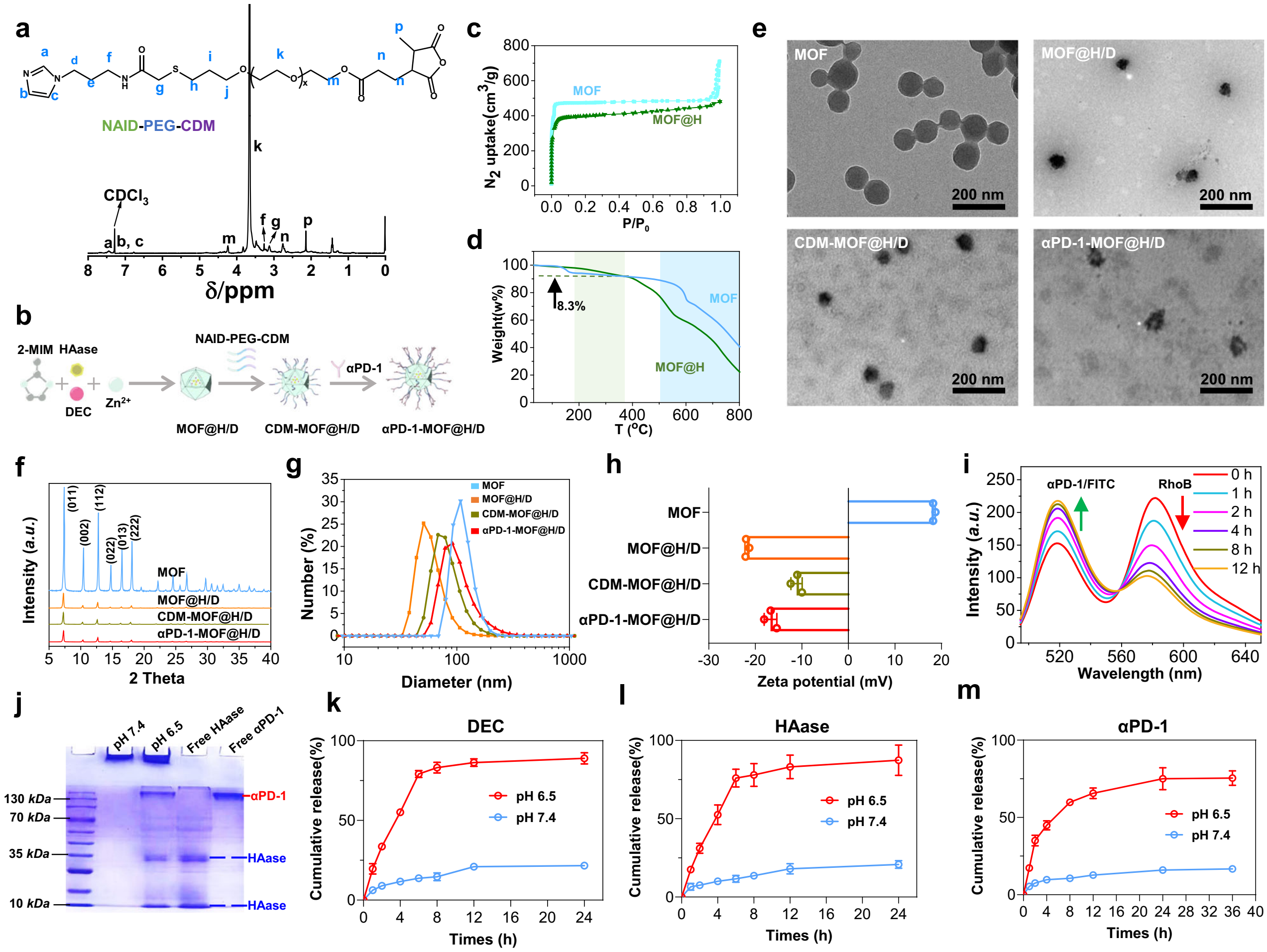

Fig. 2 | Characterizations of α-H/D. a ^{1}H nuclear magnetic resonance (^{1}H NMR) characterization of NAID-PEG-CDM. ^{1}H NMR (400 MHz, chloroform-d1, 298 K): δ(ppm) = 7.57 ppm ($-CH_2NC\boldsymbol{H}NCHCH-$ of NAID, a), 6.68–7.05 ppm ($-CH_2NCHNC\boldsymbol{H}C\boldsymbol{H}-$of NAID, b, c), 4.25 ppm ($-CH_2C\boldsymbol{H_2}OCO-$, m), 3.47–3.83 ppm ($-(C(C\boldsymbol{H_2})_2O)-$ of PEG, k), 3.27 ppm ($-CH_2C\boldsymbol{H_2}NHCO-$, f), 3.13 ppm ($-NHCOC\boldsymbol{H_2}S-$, g), 2.77 ppm ($-OCO(C\boldsymbol{H_2})_2CH-$, n), 1.93–2.27 ppm ($-CH_2CHCOOCOCH(C\boldsymbol{H_3})-$, p).The ***H*** preceded by each letter (a, b, c, etc.) denotes the specific proton whose resonance is correspondingly labeled in the ^{1}H NMR spectrum. **b** Schematic illustration of the preparation process for the nanodrug α-H/D. **c** N_2 adsorption experiments of metal–organic framework (MOF) and MOF@H. **d** The protein content of MOF@H/D was determined by thermogravimetric analysis. **e** Transmission electron microscopy (TEM) images of nanodrugs (scale bar: 200 nm). **f** Powder X-ray diffraction (PXRD) patterns of nanodrugs (a.u., arbitrary units). The particle sizes (**g**) and zeta potentials (**h**) of nanodrugs, data points represent mean ± SD (n = 3 independent experiments). **i** Fluorescence spectra of fluorescein isothiocyanate (FITC) and rhodamine B (RhoB)-labeled nanoparticle (αPD-1/FITC-MOF@RhoB) in PBS at pH 6.5 at different time points (a.u., arbitrary units). **j** Sodium dodecyl sulfate-polyacrylamide gel electrophoresis (SDS-PAGE) picture of α-H/D pretreated at pH values of 6.5 and 7.4 (0.5 µg of αPD-1 per sample; 1.4 µg of hyaluronidase (HAase) per sample). In vitro decitabine (DEC) (**k**), HAase (**l**) release from MOF@H/D, and anti-PD-1 antibody (αPD-1) (**m**) release from αPD-1-MOF@H/D at pH values of 7.4 and 6.5, data points represent mean ± SD (n = 3 independent experiments). Source data are provided as a Source data file.

L-cysteine (Cys) was stirred at room temperature, followed by the sequential addition of imidazole and zinc acetate solutions. The resulting MOF@HAase (MOF@H) was incubated with a DEC solution to obtain MOF@H/D, which was then coated with NAID-PEG-CDM to improve its stability. Finally, αPD-1 antibodies were conjugated to the PEG via a CDM linker, thereby endowing the nanoparticles with T-cell binding capability through αPD-1/PD-1 interactions. ZIF-8 frameworks are characterized by their high permeability to small molecules and structural defects caused by protein encapsulation[15]. Accordingly, N_2 adsorption experiments confirmed the porosity and structural continuity of the MOF exoskeleton during MOF@H preparation (Fig. 2c). The protein content of MOF@H was further calculated to be 8.3% (wt %) according to the weight loss within 180–360 °C via thermogravimetric analysis (Fig. 2d).

According to transmission electron microscope (TEM) images (Fig. 2e), MOF@H/D nanoparticles were spherical with a smaller average size than pristine MOFs due to crystal defects induced by protein encapsulation, which also caused discernible attenuation in the Bragg diffraction peaks (Fig. 2f). Moreover, protein loading reversed the surface charge of MOF from positive to negative and reduced the hydrodynamic size from 108 to 50.7 nm (Fig. 2g, h). Subsequent PEG coating resulted in a blurred boundary, an increased hydrodynamic size, and a shift in zeta potential from −21.3 ± 0.4 to −11.3 ± 1.2 mV, indicating the efficacious preparation of CDM-MOF@H/D. Finally, αPD-1 conjugation further increased the particle size to approximately 91.3 nm and slightly decreased the zeta potential to −16.7 ± 1.4 mV, without any noticeable alteration in morphology. Together, the above results demonstrated the successful preparation of αPD-1-MOF@H/D.

pH sensitivity and drug release behaviors in vitro

To investigate the pH-triggered release of αPD-1 via CDM linkage hydrolysis under mildly acidic conditions (pH~6.5), a fluorescence resonance energy transfer (FRET) assay was employed. αPD-1 and the nanoparticles were labeled with fluorescein isothiocyanate (FITC) and Rhodamine B (RhoB), respectively. FRET occurred when αPD-1/FITC conjugated to the MOF/RhoB, while at pH~6.5, the hydrolysis of the CDM linkage would lead to the release of αPD-1/FITC from the MOF/RhoB surface, diminishing FRET owing to the increased distance between FITC and RhoB, which resulted in amplified FITC fluorescence and attenuated RhoB fluorescence (Fig. 2i). Sodium dodecyl sulfate-polyacrylamide gel electrophoresis (SDS-PAGE) experiment further revealed pH-triggered release of αPD-1 and HAase. As shown in Fig. 2j, no electrophoretic bands for free HAase and αPD-1 could be observed at pH~7.4, indicating the stability of the prepared nanodrug under physiological conditions. In contrast, clear bands representing free HAase and αPD-1 appeared at pH~6.5, confirming the pH-dependent release of both encapsulated HAase and conjugated αPD-1.

The release profiles of DEC, HAase, and αPD-1 were quantitatively assessed at pH ~7.4 and ~6.5. As shown in Fig. 2k, l, MOF@H/D exhibited limited HAase and DEC release (<30%) at pH~7.4. In contrast, over 80% of HAase and DEC were released at pH~6.5 after 24 h, which was attributed to the protonation of imidazole moieties and the subsequent MOF disintegration. A similar pattern was observed for αPD-1 release (Fig. 2m): less than 20% αPD-1 was released from αPD-1-MOF@H/D at pH~7.4, whereas more than 75% was released at pH~6.5, indicating the robust CDM stability in neutral environments but rapid αPD-1 liberation under acidic conditions. Additionally, the enzymatic activity of HAase was evaluated, demonstrating that MOF encapsulation prolongs the activity of HAase. Notably, the MOF-encapsulated HAase maintained a nearly 60% clearance rate of hyaluronic acid (HA) after 72 h of incubation in pH~6.5 PBS (Supplementary Fig. 4).

Nanodrug-carrying TILs preparation and in vitro function assessment

TILs were obtained from subcutaneous tumors in mice on day 9 following inoculation with Panc02 cells (Fig. 3a). After positive selection by magnetic bead, more than 90% of the sorted cells were CD3-positive (Supplementary Fig. 5). Additionally, 58.9% of these $CD3^+$ TILs expressed PD-1 (Supplementary Fig. 5), which facilitates the binding of the outermost antibodies of α-H/D nanodrug to the TILs through affinity interactions. The obtained TILs were co-cultured with tumor cells and supplemented with IL-2/IL-12, leading to the significant proliferation of the TILs (Fig. 3b). To prepare nanodrug-carrying TILs, various concentrations of the nanodrug were co-incubated with TILs (Fig. 3c), and the binding efficiency was assessed using flow cytometry. As shown in Supplementary Fig. 6a, increasing the nanodrug concentration to 0.4 mg mL^{-1} did not further enhance the fluorescent intensity of the TILs. At this concentration, the T cells exhibited high viability (Supplementary Fig. 6b). Thus, 0.4 mg mL^{-1} was finally selected as the incubation concentration of the nanodrug. Confocal laser scanning microscopy (CLSM) displayed red fluorescence at the outermost layer of T cells (Fig. 3d) in this incubation concentration, indicating that the nanodrug was positioned on the cell membrane rather than being internalized. To further confirm that the binding was specifically mediated by PD-1/anti-PD-1 antibody interactions, we prepared nanoparticles surface-modified with an isotype control antibody (ISO-NPs). CLSM and scanning electron microscopy (SEM) imaging revealed that ISO-NPs did not bind to TILs (Supplementary Fig. 7). TILs were then pretreated with free α-PD-1 to block PD-1, followed by incubation with α-NPs, which also resulted in no detectable binding. In contrast, direct incubation of α-NPs with untreated TILs led to clear nanoparticle attachment to the TIL surface, as confirmed by SEM (Supplementary Fig. 7b, indicated by green arrows).

Then, the binding and release of the nanodrug from T cells at pH~7.4 and ~6.5 were investigated via CLSM. $CD8^+$ TILs were labeled with Alexa Fluor®647 (purple fluorescence), and a dual-fluorescence-visible nanodrug was created using αPD-1 labeled with Alexa Fluor®488 (green fluorescence) and RhoB (red fluorescence) instead of encapsulated drugs. As depicted in Supplementary Fig. 8a and Fig. 3e, at pH~7.4, both the green and red fluorescence signals increased over the incubation time, suggesting a gradual binding of the nanodrug to $CD8^+$ TILs due to the PD-1/αPD-1 interaction. After 24 h, RhoB fluorescence remained stable, reflecting nanoparticle retention (Supplementary Fig. 8a). However, upon adjusting the pH to 6.5, the red fluorescence on the cell membrane quickly diminished over time, indicating the detachment of the RhoB-labeled nanoparticle from $CD8^+$ TILs through CDM linkage cleavage (Fig. 3e and Supplementary Fig. 9). Flow cytometry confirmed these findings: RhoB-positive $CD8^+$ TILs accumulated steadily at pH~7.4 but decreased significantly after another 24 h of incubation at pH~6.5 (Fig. 3f, g and Supplementary Fig. 8b, c). These results suggest that the TIL-bound nanodrug could undergo detachment upon nanodrug-carrying TILs infiltrating into the TME (pH~6.5).

Subsequently, the effector functions of expanded TILs were evaluated by measuring cytokine levels in the supernatants. As shown in Fig. 3h, following co-culture with tumor cells under both pH~6.5 and ~7.4 conditions, supernatants from TIL treatments exhibited increases in tumor necrosis factor-α (TNF-α), interferon-γ (IFN-γ), and interleukin-12p70 (IL-12p70), demonstrating that the expanded TILs retained robust anti-tumor activity, largely unaffected by pH changes. Notably, cytokine levels were highest in the nanodrug-carrying TILs group, reflecting PD-1 blockade by surface-conjugated αPD-1. In contrast, conventional TILs secreted lower cytokine levels, due to PD-1/PD-L1-mediated exhaustion after chronic antigen exposure[16]. Importantly, linking nanodrug to TILs via αPD-1, which blocks PD-1/PD-L1 interactions, reactivated the anti-tumor functions of TILs, resulting in the highest cytokine secretion in the nanodrug-carrying TILs treatment group. Furthermore, there was no significant difference in cytokine levels between the pH~6.5 and ~7.4 conditions in the nanodrug-carrying TILs treatment, suggesting that αPD-1 remained on the TIL surface despite partial nanoparticle at pH 6.5 (Fig. 3e–g and Supplementary Fig. 9), thus maintaining their anti-tumor activity. Live-cell imaging and a luciferin-luciferase bioluminescence assay showed the same trend: TILs alone exhibited modest tumor killing, whereas nanodrug-carrying TILs induced substantial tumor cell death (Fig. 3i, j). Additionally, 3-(4,5-dimethylthiazol-2-yl)-2,5-diphenyltetrazolium bromide (MTT) assays demonstrated that DEC at equivalent doses showed minimal direct cytotoxicity (Supplementary Fig. 10a), suggesting that tumor cell suppression was predominantly TIL-mediated in the nanodrug-carrying TILs group.

Given that DEC has been reported to epigenetically reactivate silenced CCL5 expression in tumor cells, promoting $CD8^+$ T-cell recruitment[17], we hypothesized that after nanodrug-carrying TILs infiltrate the tumor, the release of DEC could enhance CCL5 expression in tumor cells. This, in turn, would chemotactically attract our reinfused nanodrug-carrying TILs to further infiltrate the tumor, thereby enhancing the antitumor immune response. Enzyme-linked immunosorbent assay (ELISA) results confirmed that DEC-loaded nanodrug significantly increased CCL5 secretion under simulated tumor microenvironment conditions (pH~6.5) (Supplementary Fig. 10b). Finally, we evaluated the role of HAase in improving TIL infiltration. The pancreatic cancer microenvironment is typically characterized by excessive deposition of the extracellular matrix (ECM), which our previous research has demonstrated significantly impedes immune cell infiltration into tumors[18]. Central to this matrix is hyaluronic acid (HA), which creates physical barriers that hinder antitumor immune responses[19]. By administering HAase, HA could be effectively degraded, thereby enhancing the infiltration of antitumor immune cells. Herein, we co-cultured these TILs with ex vivo Panc02 tumors and evaluated their infiltration using CLSM (Supplementary Fig. 10c). As depicted in Fig. 3k, DiI-labeled TILs (TILs/Di) incubated with excised Panc02 tumor tissue for 24 h exhibited obviously enhanced penetration when HAase was encapsulated, compared to nanodrugs without HAase. Quantitative analysis confirmed superior infiltration depths in TILs-α-H and TILs-α-H/D groups (Fig. 3l),

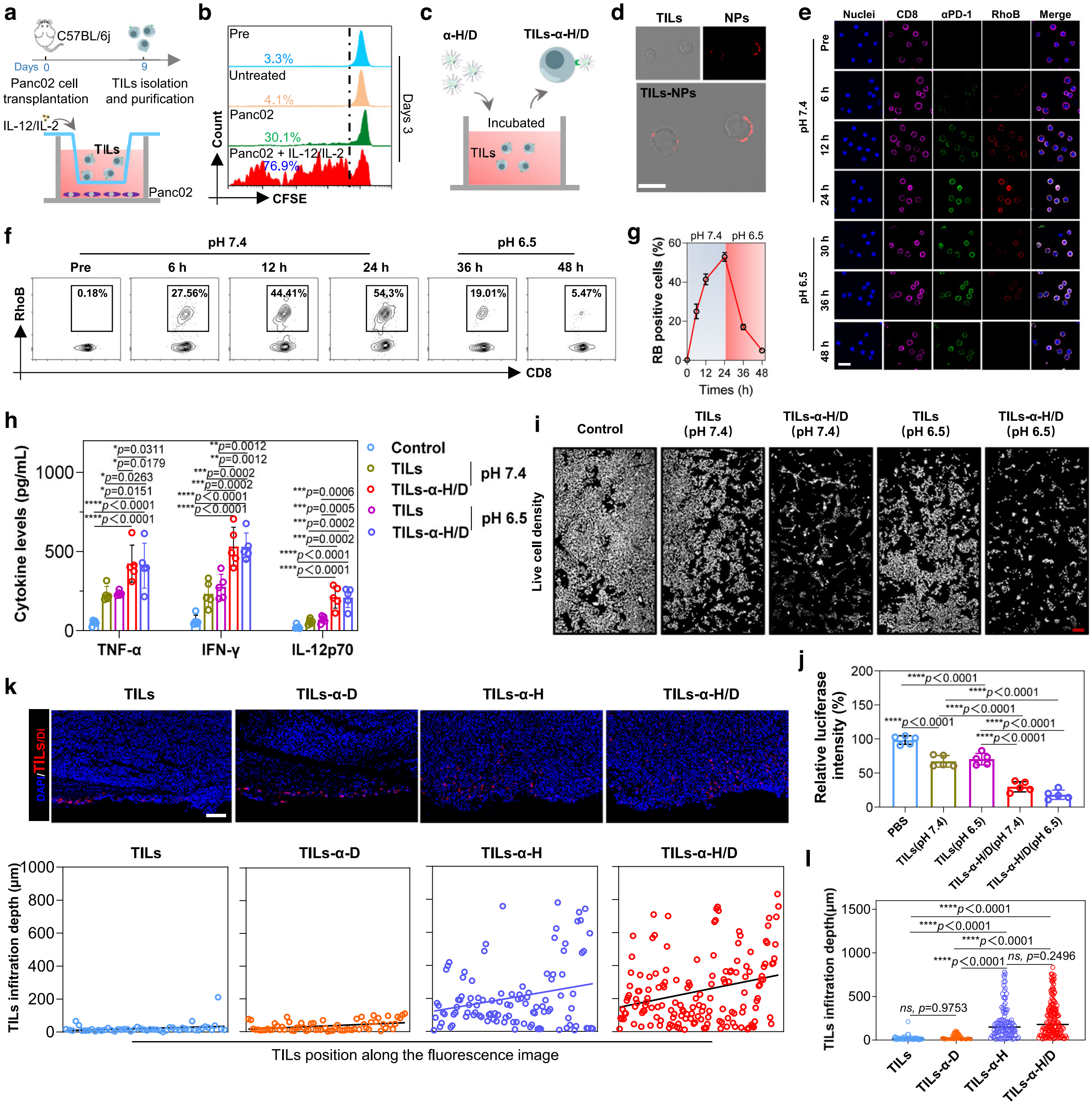

Fig. 3 | Ex vivo tumor-infiltrating lymphocytes (TILs) expansion and nanodrug-carrying TILs preparation. **a** Schematic of TIL extraction and expansion. **b** TIL proliferation analyzed by flow cytometry using carboxyfluorescein diacetate succinimidyl ester (CFSE) dilution. **c** Schematic of nanodrug-carrying TILs (TILs-α-H/D) preparation. **d** Confocal laser scanning microscope (CLSM) images of TILs-α-NPs, with rhodamine B (RhoB, red) loaded into the nanodrug for fluorescent tracing (scale bar: 10 µm). **e** CLSM of TIL binding to α-RhoB nanoparticles at pH 7.4 and RhoB nanoparticle release at pH 6.5 (scale bar: 25 µm). CD8 was labeled with Alexa Fluor®647 (purple), αPD-1 with Alexa Fluor®488 (green), and the nanoparticle with RhoB (red) (α-RhoB concentration: 0.4 mg mL^{-1}). **f** Flow cytometry results for T cell binding of α-RhoB nanoparticles at pH 7.4 and RhoB nanoparticle release at pH-6.5. **g** Quantitative flow cytometry for T cell binding and nanoparticle release at pH-7.4 and pH-6.5, data points represent mean ± SD (n = 3 independent samples). **h** Quantification of tumor necrosis factor-α (TNF-α), interferon-γ (IFN-γ), and interleukin-12p70 (IL-12p70) in supernatant 48 h post-treatment; data points represent mean ± SD (n = 5 independent samples). **i** CLSM of live cells stained with Calcein-AM (scale bar: 200 µm). **j** Relative luciferase intensity of Panc02-Luc cells after treatment, data points represent mean ± SD (n = 5 independent samples). **k** Fluorescent images and TILs infiltration depth in ex vivo tumor tissues after 24 h coculture (scale bar: 100 µm). TILs labeled with DiI (red) and nuclei with DAPI (blue). x-axis represents the position of individual TILs along the fluorescent images, from left to right. **l** Quantitative analysis of individual T cell infiltration depth in the tumor tissue, mean ± SD, n = 50 from 3 independent samples (TILs), n = 66 from 3 independent samples (TILs-α-D), n = 105 from 3 independent samples (TILs-α-H), n = 155 from 3 independent samples (TILs-α-H/D). Statistical significance was calculated using unpaired one-way ANOVA (**h**, **j**, **l**): $^{*}p < 0.05$, $^{**}p < 0.01$, $^{***}p < 0.001$ and $^{****}p < 0.0001$, ns indicates no significance. Data in (**d**, **e**) are representative of at least three independent experiments with similar results. Source data are provided as a Source data file.

demonstrating the contribution of HAase-mediated ECM degradation to improved intratumoral TIL accumulation.

In vivo distribution of nanodrug-carrying TILs

TILs are well-known for their intrinsic tumor-homing capabilities and natural ability to recognize and target tumor cells following infusion[20]. To evaluate their biodistribution, we utilized highly immunodeficient NOD-Prkdc^{em26Cd52}Il2rg^{em26Cd22}/Nju (NCG) mice to establish orthotopic pancreatic tumors and minimize the influence of endogenous immune cells. On day 5 post-model establishment, nanodrug-carrying TILs were infused, with nanoparticles loaded with the fluorescent probe 1,1′-dioctadecyl-3,3,3′,3′-tetramethylindotricarbocyanine iodide (DiR) to track in vivo distribution (Fig. 4a). As shown in Fig. 4b, c, within 36 h post-injection of the nanodrug-carrying TILs, increasing fluorescence intensity was observed at the site of the orthotopic pancreatic tumors, demonstrating the effective tumor targeting of TILs. Further ex vivo organ analysis revealed that the fluorescence intensity at the tumor site was significantly higher compared to other major organs, such as the heart, liver, spleen, lungs, and kidneys (Fig. 4d, e). These results suggest that attaching nanodrugs to TILs can leverage the superior tumor-homing properties of TILs to deliver nanodrugs to pancreatic tumors efficiently.

Since DEC-loaded nanodrugs upregulated CCL5 expression in vitro and HAase promoted TIL infiltration by degrading ECM, we hypothesized that nanodrug-carrying TILs (i.e., TILs-α-H/D) would establish a positive feedback loop in vivo. Upon infiltrating tumors, DEC would induce CCL5 expression, thereby recruiting additional nanodrug-carrying TILs, while HAase would degrade ECM barriers to facilitate further infiltration. To verify this hypothesis, we labeled TILs with DiI (TILs/Di) and collected tumor tissues at designated time points to quantify TILs infiltration using flow cytometry (Fig. 4f). As shown in Supplementary Fig. 11, on day 7 post-injection of 1×10^4 TILs, tumors treated with TILs/Di-α-H/D contained over 400 infiltrating TILs, significantly higher than groups receiving TILs alone (~68) or single-loaded formulations. Between day 7 and day 11, TIL numbers increased modestly in the TIL-only group but tripled in the TILs/Di-α-H/D group. T-distributed stochastic neighbor embedding (t-SNE) analysis further confirmed substantially increased TILs/Di infiltration in the TILs/Di-α-H/D group (Fig. 4g). Flow cytometry quantitative analysis further demonstrated that the infiltration efficiency was less than 1% in the TILs-treated group, while it reached 11.59% in the TILs/Di-α-H/D group (Fig. 4h). Moreover, ELISA showed significantly elevated intratumoral CCL5 levels in the TILs-α-H/D group compared with other groups on day 7, with further increases by day 11 (Fig. 4i). These results suggested that DEC release triggers CCL5 upregulation, creating a self-amplifying recruitment loop thatt promotes continuous accumulation of nanodrug-carrying TILs in tumors (Fig. 4j).

To better visualize intratumoral distribution, nanoparticles were dual-labeled with RhoB and green Alexa Fluor-conjugated αPD-1, and the distribution was observed via CLSM on day 7 post-injection (Fig. 4k and Supplementary Fig. 12a). As shown in Fig. 4l and Supplementary Fig. 12b, a significant colocalization of green and red fluorescence was noted within the vessels in the PBS control and TILs group after the injection of TILs-α-RhoB, with minimal fluorescence observed outside the vessels. This limited extravascular dispersion possibly is due to the enriched extracellular matrix of pancreatic cancer forming a physical barrier that hindered the permeation of nanodrug-carrying TILs outside the vessels. Remarkably, after treating tumor-bearing NCG mice with TILs-α-H/D on day 5 and subsequent injection with TILs-α-RhoB on day 7, nearly no colocalized fluorescence was detected in the vessels, suggesting that the TILs-α-H/D treatment degraded the hyaluronic acid in the extracellular matrix, thereby facilitating infused TIL penetration from the vessels into the tumor tissue. To demonstrate this, we performed immunofluorescence staining to assess HA levels within tumor tissues. As shown in Supplementary Fig. 12d, e, HA expression was reduced in the TILs-α-H/D group compared to both the PBS and TILs groups, demonstrating that intratumoral HA was effectively degraded in TILs-α-H/D–treated mice. Additionally, at sites distal to the vessels, separate green and red fluorescence signals were noted, likely due to the nanodrugs' disintegration or the cleavage of CDM bonds within the acidic tumor microenvironment, resulting in the separation of nanodrugs and TILs. This observation was further confirmed by colocalization analysis, which showed that in the control and TILs group, fluorescence was predominantly confined to the vessels, whereas in the TILs-α-H/D pretreated group, it extended beyond the vessels with minimal overlap (Fig. 4m and Supplementary Fig. 12c).

Finally, to better mimic clinical conditions, we evaluated the TIL biodistribution in immunocompetent C57BL/6j mice, which underwent cyclophosphamide myeloablation 24 h prior to drug administration. In vivo imaging demonstrated a gradual increase in tumor fluorescence intensity, peaking at 36 h after TILs-α-H/D injection (Fig. 4n, o). Ex vivo organ analysis further exhibited significantly higher fluorescence intensity in tumors than in other major organs (Fig. 4p, q), validating the tumor-targeting efficiency of nanodrug-carrying TILs in both immunodeficient and immunocompetent settings.

Therapeutic efficacy of nanodrug-carrying TILs in vivo

Encouraged by the superior tumor infiltration of TILs-α-H/D, we further assessed their tumor-suppressive effects in a subcutaneous pancreatic cancer model. Initially, a subcutaneous tumor model was established in NCG mice, which then received TILs or nanodrug-carrying TILs via tail vein injections on days 5 and 11 (Fig. 5a). As shown in Fig. 5b, c, there was no significant difference in tumor volume growth between the TILs-treated group and the control group. In contrast, treatment with TILs plus free drugs (TILs + α/H/D) or TILs carrying single agents (TILs-α-H or TILs-α-D) achieved only modest tumor suppression. In contrast, TILs-α-H/D induced marked tumor inhibition, significantly outperforming all other groups. Ex vivo tumor imaging and weight measurements further confirmed substantial tumor regression in the TILs-α-H/D groups (Fig. 5g). Consistent with these findings, TILs-α-H/D treatment prolonged survival, with no deaths observed within 47 days (Fig. 5i).

We subsequently evaluated the therapeutic efficacy of nanodrug-carrying TILs in immunocompetent C57BL/6j mice, which were preconditioned with cyclophosphamide a day prior to TILs or nanodrug-carrying TILs treatment (Fig. 5d). Similar to the results observed in NCG mice, TILs-α-H/D markedly reduced tumor growth in C57BL/6j mice (Fig. 5e, f, h), maintaining tumor volumes at 82.2 mm^3 after 40 days and extending survival with no mortalities recorded for up to 60 days (Fig. 5j). Interestingly, the TILs-α-H/D treatment appeared to have a higher tumor suppression rate in the C57BL/6j mice compared to the NCG mouse model. The analysis of tumor inhibition rates showed a greater reduction in tumor size in the C57BL/6j mice, with suppression rates of 74% in NCG mice versus 98% in C57BL/6j mice (Fig. 5k). Moreover, Hematoxylin and eosin (H&E) staining and terminal deoxynucleotidyl transferase dUTP nick end labeling (TUNEL) staining indicated that the tumor tissues in C57BL/6j mice treated with TILs-α-H/D exhibited more extensive areas of apoptosis than those in NCG mice (Fig. 5l and Supplementary Fig. 13).

Cyclophosphamide-induced immunosuppression typically begins to recover within 7–14 days in mouse models[21,22]. Therefore, we hypothesized that the enhanced tumor suppression rates observed in C57BL/6j mice reflected not only infused TIL activity but also enhanced endogenous CD8$^+$ T-cell recruitment, mediated by DEC-induced CCL5 upregulation and HAase-driven stromal remodeling. To test this hypothesis, we labeled TILs with DiI and collected tumor tissues on day 14 post-reinfusion. The tumor tissues were stained with CD8 antibodies and analyzed using CLSM. As shown in Fig. 5m and Supplementary Fig. 14, a small number of CD8$^+$ T cells (identified by green fluorescence only, representing endogenous T cells) were detected in

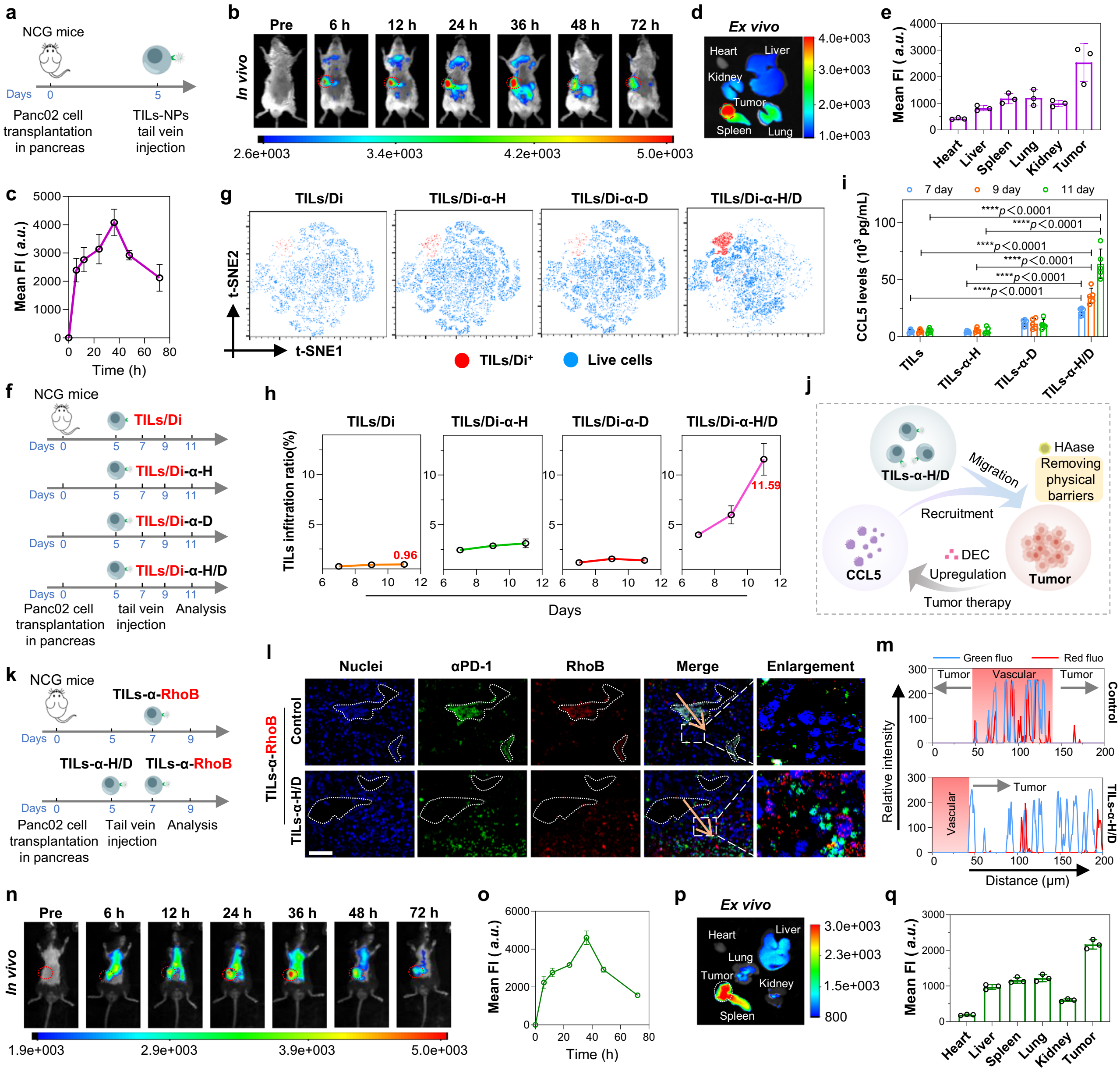

Fig. 4 | In vivo distribution of nanodrug-carrying tumor-infiltrating lymphocytes (TILs). a Experimental design for in vivo imaging using NOD-Prkdc^{em26Cd52}Il2rg^{em26Cd22}/Nju (NCG) mice. **b** In vivo 1,1′-dioctadecyl-3,3,3′,3′-tetramethylindotricarbocyanine iodide (DiR) fluorescence images after tail vein injection of nanodrug-carrying TILs in orthotopic pancreatic tumor-bearing NCG mice. **c** Quantitative fluorescence intensities (a.u., arbitrary units) in orthotopic tumors over time, data points represent mean ± SD (n = 3 mice). **d** Ex vivo images of major organs and orthotopic tumors excised 24 h post-injection. **e** Quantitative fluorescence intensities (a.u., arbitrary units) in major organs and orthotopic tumors, data points represent mean ± SD (n = 3 mice). **f** Experimental design for (**g**–**i**). **g** t-distributed stochastic neighbor embedding (t-SNE) plots of tumor flow cytometry data (red dots represent infiltrated TILs). **h** Quantification of intratumoral TILs in NCG mice, data points represent mean ± SD (n = 3 mice). **i** Quantification of C–C motif chemokine ligand 5 (CCL5) levels in tumors via enzyme-linked immunosorbent assay (ELISA), data points represent mean ± SD (n = 5 mice). **j** Diagram of cyclic recruitment of nanodrug-carrying TILs. **k** Experimental design for (**l**, **m**). **l** Confocal laser scanning microscope (CLSM) images of tumor sections showing colocalization of nanodrug (RhoB, red) and αPD-1 (Alexa Fluor®488, green) on T cells after tail vein injection (scale bar: 100 μm), nuclei stained with 4′,6-diamidino-2-phenylindole (DAPI, blue). **m** Fluorescence intensity profiles across the selected line in (**l**). **n** In vivo DiR fluorescence imaging in C57BL/6j mice. **o** Quantitative fluorescence intensities (a.u., arbitrary units) in orthotopic pancreatic tumors at various time points post-injection, data points represent mean ± SD (n = 3 mice). **p** Ex vivo DiR fluorescence imaging of major organs and orthotopic tumors excised 24 h post-injection. **q** Quantitative analysis of fluorescence intensities (a.u., arbitrary units) in major organs and orthotopic tumors, data points represent mean ± SD (n = 3 mice). Statistical significance was calculated using unpaired one-way ANOVA: $^{****}p < 0.0001$. Data in (**l**) are representative of three independent experiments with similar results. Source data are provided as a Source data file.

PBS-treated C57BL/6j mice, suggesting partial immune recovery from cyclophosphamide-induced immunosuppression. Both NCG and C57BL/6j mice treated with TILs-α-H/D showed substantial infiltration of Di-labeled TILs (red fluorescence), which was greater than that observed in the TILs group. Notably, in NCG mice, most CD8$^+$ T cells were Di$^+$, indicating that they were primarily infused TILs rather than endogenous T cells. In contrast, C57BL/6j mice exhibited both a large number of Di$^+$ TILs and a substantial population of CD8$^+$ T cells labeled solely by green fluorescence, indicating successful recruitment of endogenous CD8$^+$ T cells following immunosuppression recovery. These findings were further supported by flow cytometry analysis. In the C57BL/6j mice receiving TILs/Di-α-H/D treatment, approximately

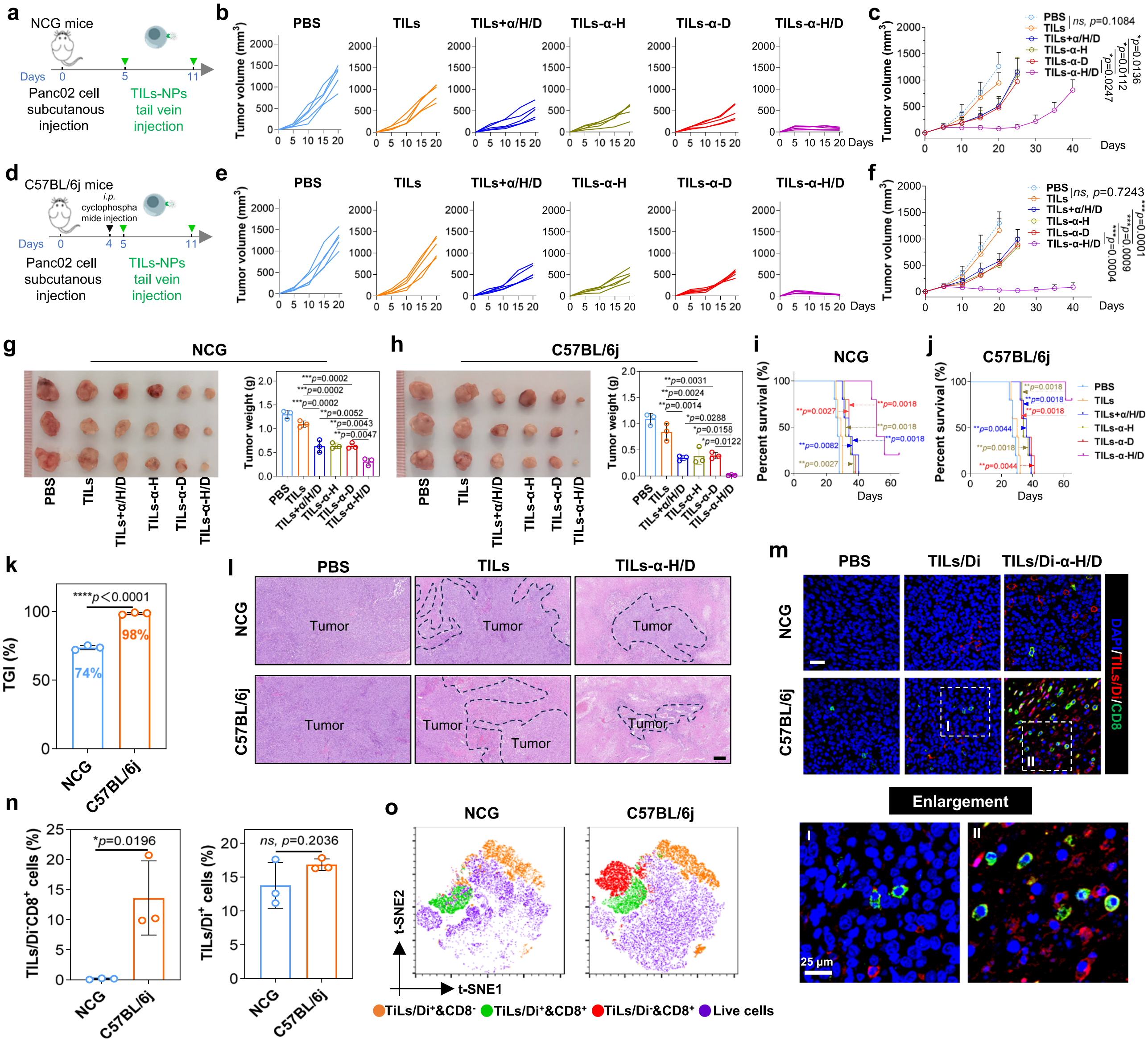

Fig. 5 | Effect of antitumor and immune regulation in vivo. a Schematic of the experimental design for the antitumor study in NOD-Prkdc^{em26Cd52}Il2rg^{em26Cd22}/Nju (NCG) mice. **b** Individual tumor growth curves for Panc02 tumor-bearing NCG mice receiving different treatments. **c** Tumor growth in Panc02 tumor-bearing NCG mice, data points represent mean ± SD (n = 5 mice). **d** Experimental design for the antitumor study in C57BL/6j mice, with cyclophosphamide intraperitoneal injection (200 mg kg^{-1}). **e** Individual tumor growth curves for Panc02 tumor-bearing C57BL/6j mice receiving different treatments. **f** Tumor growth in Panc02 tumor-bearing C57BL/6j mice, data points represent mean ± SD (n = 5 mice). **g** Images of subcutaneous tumors and tumor weights from Panc02 tumor-bearing NCG mice after 20 days, data points represent mean ± SD (n = 3 mice). **h** Images of subcutaneous tumors and tumor weights from Panc02 tumor-bearing C57BL/6j mice after 20 days, data points represent mean ± SD (n = 3 mice). **i** Cumulative survival of NCG mice, n = 5 mice. **j** Cumulative survival of C57BL/6j mice, n = 5 mice. **k** Tumor growth inhibition (%) in NCG and C57BL/6j mice treated with nanodrug-carrying TILs, data points represent mean ± SD (n = 3 mice). **l** Hematoxylin and eosin (H&E) staining of tumor tissues at 20 days, tumor margins marked with a dotted line (scale bar: 200 μm). **m** Confocal laser scanning microscope (CLSM) images of tumor sections showing TILs and CD8$^+$ T cells. Red fluorescence: TILs, green fluorescence: CD8$^+$ T cells, blue fluorescence: nuclei (scale bar: 50 μm). **n** Quantification of TILs and CD8$^+$ T cells in tumor tissue from NCG and C57BL/6j mice, data points represent mean ± SD (n = 3 mice). **o** t-distributed stochastic neighbor embedding (t-SNE) plots of flow cytometry data from tumor samples in NCG and C57BL/6j mice treated with TILs-α-H/D. Red dots: endogenous CD8$^+$ T cells, green/orange dots: exogenous TILs. Statistical significance was calculated using unpaired one-way ANOVA (**c**, **f**, **g**, **h**), two-sided unpaired *t*-test (**k**, **n**), and log-rank (Mantel–Cox) test (**i**, **j**): $^*p < 0.05$, $^{**}p < 0.01$, $^{***}p < 0.001$ and $^{****}p < 0.0001$, ns indicates no significance. Source data are provided as a Source data file.

15% of the CD45$^+$ cells were exogenous Di$^+$ TILs, and 20% were Di$^-$CD8$^+$ endogenous T cells (Supplementary Fig. 15). Quantitative flow cytometry revealed similar proportions of Di$^+$CD45$^+$ cells in both NCG and C57BL/6j tumors, but Di$^-$CD8$^+$ T cells reached 10% only in C57BL/6j mice (Fig. 5n). t-SNE analysis further revealed extensive infiltration of infused TILs (orange and green dots) in tumor tissues from both mouse strains, whereas a notable population of endogenous CD8$^+$ T cells (red dots) was only observed in C57BL/6j mice (Fig. 5o). These results indicate that nanodrug-loaded TILs not only deliver infused TILs effectively but also potentiate endogenous T-cell responses following immune recovery.

The antitumor efficacy of nanodrug-carrying TILs was further assessed in an orthotopic C57BL/6j mouse model of pancreatic tumors. Mice were randomly divided into four groups: PBS, TIL-α-H, TIL-α-D, and TIL-α-H/D. Each group received intravenous injections on days 5 and 11, with tumor growth monitored via magnetic resonance imaging (MRI) (Fig. 6a). Consistent with subcutaneous results, TIL-α-H/D exhibited the greatest tumor growth inhibition (Fig. 6b–d). Similarly,

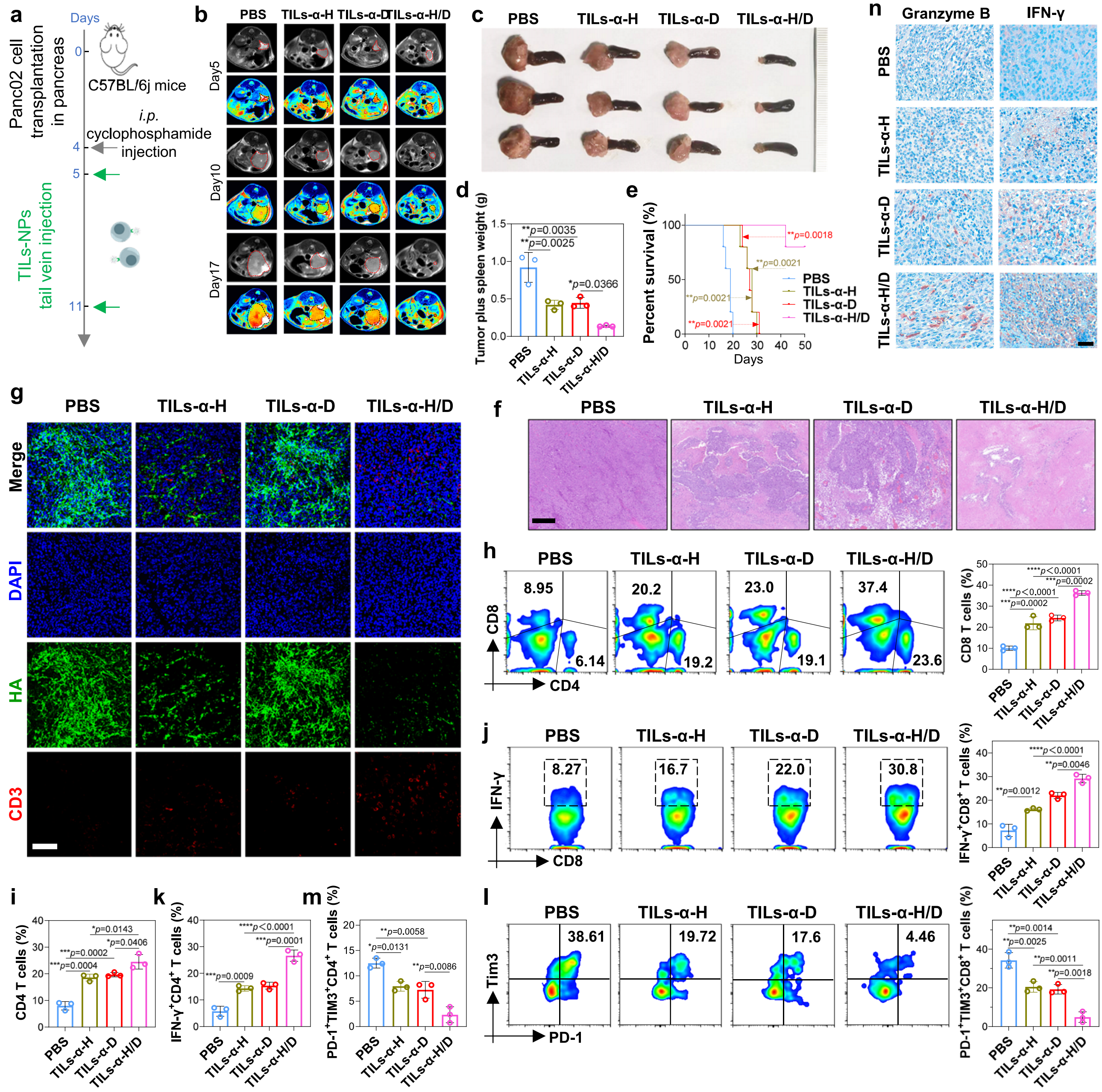

Fig. 6 | Antitumor efficacy of treatments in an orthotopic Panc02 pancreatic tumor model in C57BL/6j mice. **a** Schematic of the experimental design for the antitumor study in C57BL/6j mice. **b** Tumor growth was monitored by magnetic resonance imaging (MRI) at 5, 10, and 17 days post-treatment initiation. **c** Representative photographs of excised orthotopic pancreatic tumors and spleens from each treatment group. **d** Weights of tumors and spleens at the study endpoint, data points represent mean ± SD (n = 3 mice). **e** Cumulative survival of mice bearing orthotopic tumors after different treatments, n = 5 mice. **f** Hematoxylin and eosin (H&E) staining of tumor tissues, scale bar: 200 µm. **g** Double immunofluorescence for hyaluronic acid (HA) and $CD3^+$ T cells in tumor sections, HA (labeled with Alexa Fluor®488, green), $CD3^+$ T cells (labeled with Alexa Fluor®555, red), nuclei (stained with 4′,6-diamidino-2-phenylindole (DAPI), blue), scale bar: 100 µm. **h** Flow cytometry quantification of $CD8^+$ T cells (gated on $CD3^+$ T cells) in orthotopic tumors, data points represent mean ± SD (n = 3 mice). **i** Quantification of $CD4^+$ (gated on $CD3^+$ T cells) T cells in tumors, data points represent mean ± SD (n = 3 mice). **j** Flow cytometry analysis of $CD8^+IFN\text{-}\gamma^+$ T cells (gated on $CD3^+CD4^-CD8^+$ T cells) in tumors, data points represent mean ± SD (n = 3 mice). **k** Quantitative analysis of $CD4^+IFN\text{-}\gamma^+$ T cells (gated on $CD3^+CD4^+CD8^-$ T cells) in tumors, data points represent mean ± SD (n = 3 mice). **l** Flow cytometry analysis of exhausted $CD8^+$ TILs ($PD\text{-}1^+Tim3^+CD8^+$; gated on $CD3^+CD4^-CD8^+$ T cells), data points represent mean ± SD (n = 3 mice). **m** Quantification of exhausted $CD4^+$ TILs ($PD\text{-}1^+Tim3^+CD4^+$; gated on $CD3^+CD4^+CD8^-$ T cells), data points represent mean ± SD (n = 3 mice). **n** Immunohistochemical staining of granzyme B and interferon-γ (IFN-γ) in tumor tissues, scale bar: 50 µm. Statistical significance was calculated using unpaired one-way ANOVA (**d**, **h**, **i**, **j**, **k**, **l**, **m**), and log-rank (Mantel–Cox) test (**e**): $*p < 0.05$, $**p < 0.01$, $***p < 0.001$ and $****p < 0.0001$. Source data are provided as a Source data file.

while TILs carrying single agents showed moderate survival benefit, dual-loading with HAase and DEC provided the most significant extension in survival (Fig. 6e). Additionally, H&E and TUNEL staining revealed that the tumor tissues from mice treated with TIL-α-H/D exhibited more extensive areas of apoptosis than those in other groups (Fig. 6f and Supplementary Fig. 16).

In vivo immune modulation by nanodrug-carrying TILs

To investigate how nanodrug-carrying TILs remodel the tumor immune microenvironment, we first assessed $CD3^+$ T cell infiltration and HA deposition by immunofluorescence staining and confocal microscopy. As shown in Fig. 6g and Supplementary Fig. 17, HA levels were significantly lower in the tumor tissues of mice treated with

HAase-loaded nanodrug-carrying TILs compared to those in the PBS and TIL-α-D groups. This reduction likely resulted from the infiltration of HAase-bearing TILs into the tumor, where they released HAase in response to the tumor microenvironment, facilitating local stromal degradation. Furthermore, the TIL-α-H/D group exhibited the lowest HA expression, consistent with enhanced infiltration efficiency leading to greater HAase delivery. Additionally, TIL infiltration also varied across treatment groups. Both TIL-α-H and TIL-α-D groups demonstrated modest increases in $CD3^+$ T-cell density compared to the PBS control. Strikingly, TIL-α-H/D achieved the highest $CD3^+$ T-cell infiltration, likely attributable to synergistic effects of stromal degradation and CCL5-driven recruitment.

To directly determine whether $CD3^+$ T cell recruitment was driven by DEC-induced upregulation of CCL5, we established a stable *CCL5* knockdown (KD) Panc02 cell line via lentiviral transduction with *CCL5*-targeting short hairpin RNA (shRNA) and green fluorescent protein (GFP) co-expression. Successful knockdown was validated by clearly observed GFP fluorescence and significantly reduced CCL5 protein levels confirmed by western blot analysis (Supplementary Fig. 18a). For in vivo testing, wild-type Panc02 cells and Panc02/*CCL5* KD cells were simultaneously inoculated into opposite hindlimbs of the same C57BL/6j mouse, followed by PBS or TILs-α-H/D treatment (Supplementary Fig. 18b). As shown in Supplementary Fig. 18c–e, tumors derived from Panc02/*CCL5* KD cells exhibited significantly accelerated growth compared to Panc02 tumors under TILs-α-H/D treatment. ELISA further confirmed a significant decrease in intratumoral CCL5 levels in the *CCL5* KD tumors (Supplementary Fig. 18f). Moreover, immunofluorescence staining revealed substantially fewer infiltrating $CD3^+$ T cells in Panc02/*CCL5* KD tumors than in Panc02 tumors after TILs-α-H/D treatment (Supplementary Fig. 18g). Collectively, these results demonstrate that DEC-induced CCL5 upregulation is a key mechanism driving $CD3^+$ T cells recruitment into tumors.

To further identify the specific subpopulations infiltrating orthotopic pancreatic tumors, we isolated lymphocytes from the tumors and analyzed them using flow cytometry. As shown in Fig. 6h, i, the TIL-α-H and TIL-α-D treatment groups exhibited limited infiltration of $CD4^+$ and $CD8^+$ T cells infiltrating the tumors. Conversely, the TIL-α-H/D group showed a significantly higher infiltration of these cells compared to groups treated with TILs carrying either HAase or DEC alone. We next assessed T-cell functional activation by quantifying $CD3^+IFN\text{-}\gamma^+$ effector cells using flow cytometry. As shown in Fig. 6j, k and Supplementary Fig. 19a, the TIL-α-H and TIL-α-D treatments increased the percentage of $CD4^+$ and $CD8^+$ T cells expressing IFN-γ, with the TIL-α-H/D treatment yielding the highest percentage of these cells. Furthermore, we evaluated the exhaustion status of intratumoral TILs. As shown in Fig. 6l, m, and Supplementary Fig. 19b, the TIL-α-H/D treatment group exhibited the lowest proportion of exhausted TILs—including exhausted $CD4^+$ T cells ($PD\text{-}1^+Tim3^+CD4^+$) and $CD8^+$ T cells ($PD\text{-}1^+Tim3^+CD8^+$)—among all treatments. Consistently, immunohistochemical analysis revealed that TIL-α-H/D treatment resulted in the strongest upregulation of granzyme B and IFN-γ expression compared with other groups (Fig. 6n and Supplementary Fig. 20).

Anti-metastatic efficacy and biosafety of nanodrug-carrying TILs

Pancreatic cancer is notably metastatic, contributing substantially to the high mortality rate among patients[23]. To assess the efficacy of nanodrug-carrying TILs in inhibiting metastasis and invasion of pancreatic cancer, we utilized a systemic metastasis model by injecting Panc02 cells into the tail veins of C57BL/6j mice. Four days post-injection, mice underwent myeloablation with cyclophosphamide, followed by intravenous administration of nanodrug-carrying TILs (Fig. 7a). The progression of metastases was monitored by the bioluminescence of Panc02 cells in vivo. As shown in Fig. 7b, c, the PBS-treated group displayed rapid cancer progression, with strong bioluminescence signals and early mortality by day 17. Treatment with TILs-α-H or TILs-α-D exhibited significantly attenuated bioluminescence, whereas TILs-α-H/D showed the slowest tumor dissemination and markedly weaker bioluminescence signals on day 17 compared to single-agent groups. Correspondingly, survival analysis demonstrated that TILs-α-H/D conferred the greatest survival benefit among all treatment groups (Fig. 7d).

H&E staining of major organs revealed numerous tumor nodules in the lungs, liver, and kidneys of PBS-treated mice (Fig. 7e), while hearts and spleens were largely unaffected (Supplementary Fig. 21). In comparison, mice treated with TILs carrying either HAase or DEC alone exhibited significantly fewer metastatic nodules. Notably, organs from the TILs-α-H/D group displayed almost complete absence of metastases. Quantitative analysis confirmed that TILs-α-H/D achieved the lowest metastatic burden among all groups (Fig. 7f). These results demonstrate that TILs-α-H/D effectively inhibit pancreatic cancer metastasis and prevent the formation of metastatic foci in vital organs such as the lungs, liver, and kidneys (Fig. 7g). Additionally, to assess spontaneous metastasis in the orthotopic pancreatic cancer model, histological analysis of lung tissues was conducted. As shown in Supplementary Fig. 22, no metastatic lesions were detected in the lungs of mice treated with TIL-α-H/D at either day 20 or day 30, underscoring the superior efficacy of TIL-α-H/D in preventing spontaneous metastasis.

Compared to other ACT therapies, such as CAR-T and TCR-T, TIL therapy typically requires a larger T-cell dose[24]. This large-scale infusion can potentially trigger excessive immune responses, including cytokine release syndrome. Recognizing the enhanced infiltration efficiency of nanodrug-carrying TILs, we opted for a significantly lower dose of 10^6 cells, in contrast to the dosages of ~10^7 cells per mouse reported in other studies[16,25], to evaluate tumor inhibition effects. This reduced dose potentially can offer greater safety. To verify this, we infused TILs intravenously into non-tumor-bearing C57BL/6j mice and measured serum cytokines associated with CRS (IL-6 and TNF-α) using ELISA (Fig. 7h). As shown in Fig. 7i, j, cytokine levels showed only mild, nonsignificant increases compared to PBS controls, indicating a favorable safety profile. Further serum biochemical analysis revealed no significant differences in liver function markers (i.e., alanine aminotransferase (ALT), total bilirubin (TBIL)) and kidney function indicators (i.e., UREA, creatinine (CREA)) between the treated groups and the control (Fig. 7k–n), further confirming the good biosafety of nanodrug-carrying TILs.

Discussion

The efficacy of TIL therapy against solid tumors is no longer merely conceptual, as evidenced by the FDA's accelerated approval of Iovance's lifileucel for melanoma in February 2024[26]. Encouraged by this success, TIL therapy is now being explored in other solid cancer types, such as recurrent cervical cancer (NCT04766320)[27] and metastatic lung cancer (NCT03215810)[28]. To further enhance efficacy, next-generation TIL products is endeavoring to incorporate other sophisticated manipulations, including genetic engineering to improve trafficking, persistence, and effector function[29]. For instance, overexpressed chemokine receptors such as C-X-C chemokine receptor type 6 (CXCR6) has been proposed to optimize TIL infiltration in pancreatic cancer[30]. However, genetic modification raises safety, ethical, and logistical challenges, including off-target toxicity, manufacturing complexity, and regulatory barriers.

In this context, nanoengineering provides a compelling, modular alternative to enhance TIL functionality without genomic manipulation. Nanocarriers can stabilize, solubilize, and locally retain therapeutic cargos[31–33], overcoming the rapid diffusion of naked agents even after direct intratumoral or peritumoral administration[34,35]. Importantly, TILs' inherent tumor-homing ability can concentrate therapeutic agents at tumor foci, further increasing the accumulation

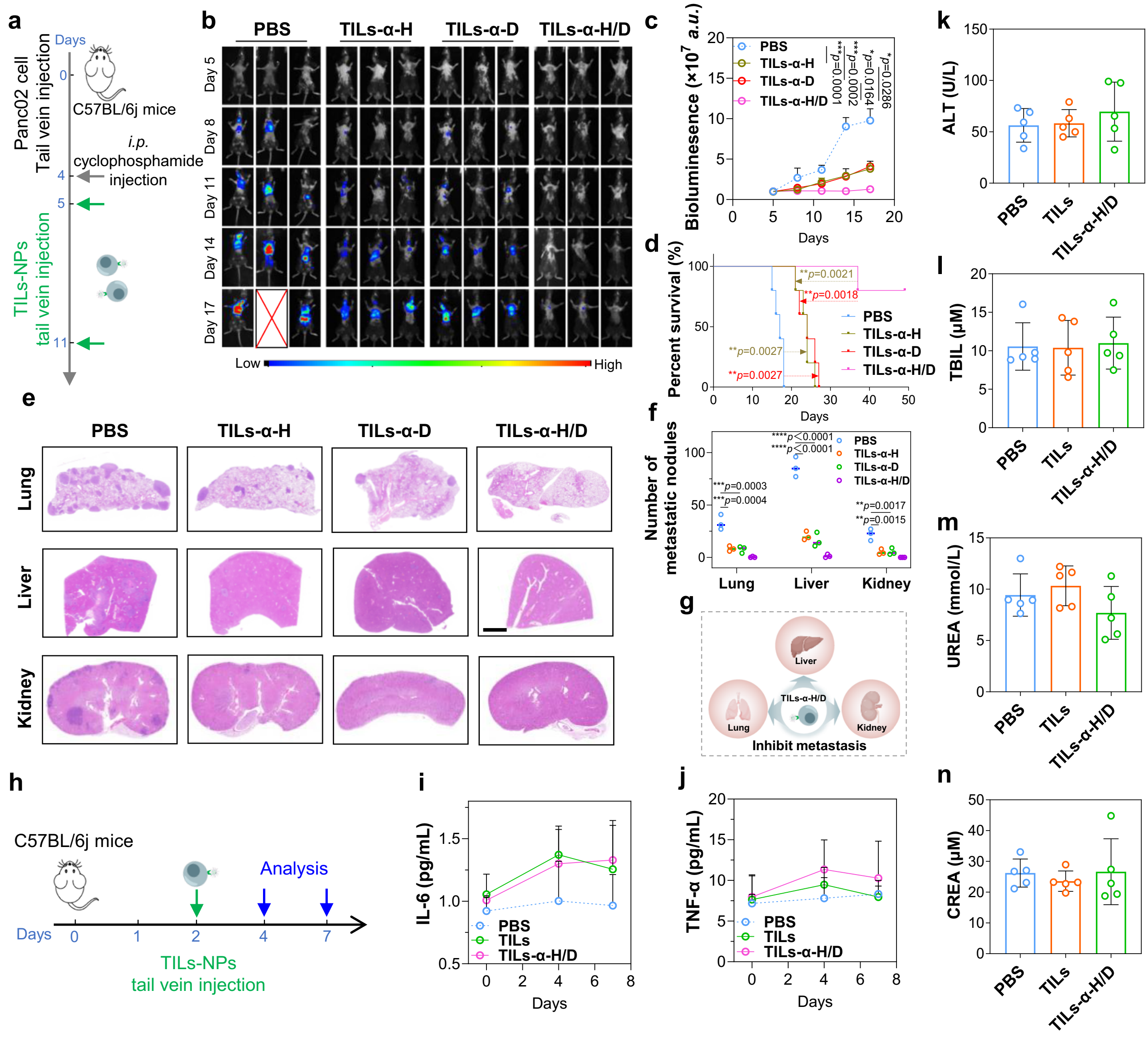

Fig. 7 | Anti-metastatic efficacy and safety assessments of the nanodrug-carrying TILs. a Schematic representation of the anti-metastasis tumor study schedule in C57BL/6j mice. **b** In vivo bioluminescence imaging in the Panc02-Luc metastatic tumor mice. **c** Quantitation of whole-body bioluminescence (a.u., arbitrary units), data points represent mean ± SD (n = 3 mice). **d** Survival curves of mice receiving different treatments, n = 5 mice. **e** Hematoxylin and eosin (H&E) staining of major organs, including the lung, liver, and kidney, scale bar: 0.2 mm. **f** The number of metastatic foci in the lung, liver, and kidney, data points represent mean ± SD (n = 3 mice). **g** Nanodrug-carrying TILs inhibit metastasis in multiple organs in mouse metastasis models. **h** Schematic representation of the safety assessments of nanodrug-carrying TILs. Interleukin-6 (IL-6) (**i**) and tumor necrosis factor-α (TNF-α) (**j**) levels in serum from mice post different treatments, data points represent mean ± SD (n = 3 mice). Serum biochemical parameters with functional annotations: alanine aminotransferase (ALT) (**k**) measuring hepatocellular injury, total bilirubin (TBIL) (**l**) reflecting hepatobiliary function, urea (UREA) (**m**) indicating renal filtration and metabolic status, and creatinine (CREA) (**n**) assessing glomerular filtration rate; data presented as mean ± SD (n = 5 mice). Statistical significance was calculated using unpaired one-way ANOVA (**c**, **f**) and log-rank (Mantel–Cox) test (**d**): $^{*}p < 0.05$, $^{**}p < 0.01$, $^{***}p < 0.001$ and $^{****}p < 0.0001$. Source data are provided as a Source data file.

of their therapeutic effects[36]. Such convergence of nanoengineering and TIL therapy provides a flexible platform: once optimized, the same framework can integrate diverse drug combinations tailored to tumor-specific barriers while avoiding irreversible genetic alterations.

Building on this concept, we designed nanoengineered TILs to address two major challenges in immune-resistant pancreatic cancer: insufficient TIL infiltration and suppressed antitumor activity within the highly fibrotic and immunosuppressive TME. We engineered a self-directed nanodrug-TIL system, tethering αPD-1-conjugated MOF nanocarriers loaded with HAase and the small-molecule drug DEC ("CCL5 replenisher") onto the TIL surface. This multifunctional "backpack" promotes TIL infiltration by degrading stromal barriers, enhances local chemokine-driven recruitment of both infused and endogenous T cells, and simultaneously relieves PD-1-mediated exhaustion. This combinational design demonstrated profound benefits. Even when only a minor fraction of infused TILs reached early tumor foci, the self-amplifying recruitment loop enabled sustained infiltration into otherwise inaccessible tumor parenchyma. In orthotopic pancreatic tumors, 11.59% of nanoengineered TILs accumulated locally versus only 0.96% for free TILs (Fig. 4h). Concurrently, αPD-1 blockade reinvigorated exhausted TILs, fully unleashing their antitumor potency. Strikingly, in immunocompetent mice, nanoengineered TILs also recruited endogenous CD8^{+} T cells and thus achieving a much more impressive tumor growth inhibition rate (98%), substantially outperforming the 74% suppression observed in immunodeficient NCG models (Fig. 5k). These results further underscore the translational advantage of this system: mobilizing both adoptively transferred and host-derived immune responses, which often rapid recover after lymphodepletion[37] to maximize antitumor effects.

Another noteworthy improvement achieved in this study is the significant therapeutic outcomes obtained with a modest dose of nanoengineered TILs (1×10^6 cells), a dosage at which non-engineered TILs showed few effects. Based on FDA interspecies extrapolation guidelines[37], this corresponds to 1.95×10^8–2.43×10^8 TILs for a 60 kg human patient. While the standard dosage of TILs for pancreatic cancer remains undetermined yet, referencing the FDA-recommended lifileucel doses for melanoma (7.5×10^9–72×10^9 viable cells) reflects the great potential of our system to substantially reduce TIL dosing by up to one or two orders of magnitude compared to traditional TIL therapy. We envision this reduction could improve safety, accelerate manufacturing timelines, and expand patient accessibility, especially for terminal-stage cases requiring rapid intervention. Moreover, given the scarcity of original effector lymphocytes in immunologically "cold" tumors[10,38], it is of equal importance in future exploration to develop advanced ex vivo manufacturing and expansion techniques to meet therapeutic dosage requirements. Since the MOF nanocarrier devised here is conducive to protein loading, it is fairly conceivable to utilize this system for combining supporting cytokines (e.g., IL-2, IL-12, or IL-15) to realize in situ expansion of TILs in the near future.

To date, the optimal timing of implementing TIL therapy is still pending, particularly in relation to ICB therapy. TIL therapy is typically deployed after ICB failure[39]. But prior PD-1 blockade might compromise the neoantigen reactivity of TILs, potentially leading to therapeutic resistance[40,41]. By employing αPD-1 antibodies as both functional inhibitors and tethering ligands, our approach synchronizes TIL and ICB therapies. The engineered backpacks provide tumor-responsive, pH-triggered release of nanocarriers and drugs, integrating checkpoint blockade directly into TIL delivery while bypassing sequencing dilemmas. Compared to other commonly used backpacking methods (e.g., physical adsorption or covalent coupling)[42]. This αPD-1-mediated tethering offers a stable, reproducible, and minimally disruptive approach that preserves TIL membrane integrity and functional plasticity[42,43]. Furthermore, as the high flexibility of this formulation allows incorporation of various therapeutic agents (not limited to small molecule drugs, proteins, and RNA), its application scope is bound to extend far beyond the pancreatic cancer illustrated here.

Despite these encouraging results, two limitations of our study should be clarified here. First, while approximately 15–20% of PDAC patients undergo surgical resection, the majority only receive diagnostic biopsies[44,45]. Ensuring sufficient TIL yield from limited biopsy samples remains a potential constraint. Encouragingly, emerging biopsy-derived TIL (bTIL) protocols have demonstrated recovery of $>5 \times 10^6$ functional TILs from core-needle biopsies in melanoma, with comparable phenotypic and functional profiles to those obtained from surgical resections[46]. Some of these approaches are already being evaluated in clinical trials (e.g., NCT05470283). Extending and optimizing these protocols for PDAC may expand patient eligibility. Second, the TILs used here were derived from a rapidly established murine tumor model, which may not fully reflect the exhaustion states of TILs in long-standing human PDAC. While T-cell dysfunction programs often initiate within the first 1–2 weeks of tumorigenesis[47–49], human TILs experience more chronic and multifactorial exhaustion. Future studies should therefore validate this strategy in longer-established murine models or patient-derived xenografts to strengthen clinical translatability.

In summary, we developed a nanoengineered TIL platform integrating αPD-1-conjugated MOF nanocarriers carrying HAase and DEC, enabling self-amplifying infiltration and synchronized checkpoint blockade in pancreatic cancer. This strategy achieved robust tumor suppression, enhanced endogenous T cell recruitment, and prolonged survival, even with significantly reduced TIL doses. By lowering the therapeutic threshold and offering a versatile, modular formulation, this αPD-1-based backpacking strategy may hold promise for shifting TIL therapy earlier in the treatment continuum, either as a standalone approach or in synergy with ICB or standard-of-care chemotherapy. Given its adaptability, this platform holds potential for extension across diverse solid tumor types, paving the way toward next-generation adoptive T cell therapies.

Methods

The synthesis of COOH-PEG-OH

Five grams APEG-OH was dissolved into 48 mL DMA, the solution was bubbled for 20 min to remove O_2. Then, 3.84 g 3-mercaptopropionic acid and 1.71 g 2,2′-azobis(2-methylpropionitrile) were added to the solution. The mixture was kept in an oil bath at 65 °C for 24 h. COOH-PEG-OH was purified by precipitation into diethyl ether three times. The product was dried under a vacuum to obtain a white solid.

The synthesis of NAID-PEG-OH

0.5 g COOH-PEG-OH was dissolved in 5 mL dichloromethane (DCM), followed by the addition of 0.319 g EDCI and 0.192 g NHS. The above mixture was stirred for 4 h. The DMSO solution of NAID was then added to the above solution. After 24 h of reaction, the mixture was poured into a large amount of diethyl ether. The white precipitate was centrifugated and isolated from the supernatant, achieving the crude product. The crude product was then dissolved in DCM and purified as described above two times to obtain NAID-PEG-OH.

The synthesis of NAID-PEG-CDM

0.15 g CDM was dissolved in 5 mL anhydrous DCM, into which 30 μL dry DMF was added. 1.05 g oxalyl chloride was dissolved in dry DCM and then added to the CDM solution. The mixture was stirred for 6 h in the dark. The remained oxalyl chloride was removed alongside the removal of the solvent. 0.275 g NAID-PEG-OH was dissolved in 5 mL dry DCM, into which 0.053 g TEA, 0.051 g DMAP, and the above activated CDM were added. The whole processes were conducted in an ice bath. The mixture was then transferred into a separatory funnel. The organic phase was washed by isopycnic saturated ammonium chloride solution and saturated sodium chloride solution. The organic phase was then isolated and dried by anhydrous $MgSO_4$. After the removal of $MgSO_4$, the organic phase was poured into a large amount of diethyl ether. The precipitate was then isolated and dissolved in DCM, achieving the crude product. The crude product was then purified as described above two times to obtain the final NAID-PEG-CDM.

Characterization

Powder X-ray diffraction (PXRD) patterns were collected (0.02 o/step, 0.06 s/step) on a Bruker D8 Advance diffractometer (Cu Kα) at room temperature. N_2 adsorption isotherms were collected with a JW-DX surface area analyzer at −196 °C. All the samples were pretreated under 100 °C for 12 h before measurements. Thermogravimetric analyses (TGA) were performed under an N_2 atmosphere (20 mL min^{-1}) with temperature increasing at 10 °C min^{-1} using a TA-Q50 system. The samples were dried in vacuo at 100 °C for 12 h before TGA analysis. Transmission electron microscopy (TEM) observations were conducted on a JEOL1400 plus electron microscope at an acceleration voltage of 120 kV. The sample solution was deposited onto a carbon-coated copper grid, and the solvent was completely evaporated under an infrared lamp before TEM observation. The hydrodynamic diameter, size distribution of nanoparticles, and zeta potentials of nanoparticles were measured using the Zeta-Nanosizer (ZEN3600, Malvern Instruments Ltd, Worcestershire, UK), which was routinely calibrated with a −50 mV Zeta-potential standard (Malvern Instruments). To observe the binding between TILs and nanodrugs, TILs were treated with various formulations, including ISO-NPs, α-PD-1 block + α-NPs, and α-NPs. The cells, collected by centrifugation, were fixed with glutaraldehyde for 30 min, followed by dehydration through a gradient ethanol series and subsequent transfer to glass slides. After gold sputter-coating, the cell samples were analyzed using a field-emission scanning electron microscope (Gemini SEM500, Carl Zeiss, Germany) to visualize the binding of TILs to nanodrugs.

The preparation of α-H/D nanoparticle

Five hundred microliters aqueous solution of HAase (20 mg mL^{-1}), 400 μL aqueous solution of PVP (50 mg mL^{-1}), and 500 μL aqueous solution of Cys (10 mg mL^{-1}) were mixed at room temperature. Then, a 20 mL aqueous solution of 2-MIM (160 mM) was added to the above mixture, followed by the addition of 10 mL aqueous solution of zinc acetate (50 mM). MOF@H was obtained after 10 min of stirring. The above dispersion of MOF@H was centrifuged to remove the free components in the supernatant. The isolated MOF@H was washed twice with water, achieving MOF nanoparticles encapsulating HAE (MOF@H). The above-prepared MOF@H was dispersed in 1.8 mL DMSO, into which 200 μL DMSO solution of DEC (10 mg mL^{-1}) was added. After incubation in the dark for 4 h, the dispersion was centrifuged, and the MOF nanoparticles encapsulating both HAE and DEC (MOF@H/D) were isolated and washed with water for further use. The obtained MOF@H/D was dispersed in an aqueous solution containing NAID-PEG-CDM. After stirring overnight, the functional NAID-PEG-CDM was coated on the MOF@H/D surface. Free NAID-PEG-CDM was removed after centrifugation and washing. The obtained CDM-MOF@H/D was then dispersed in PBS, followed by the addition of an aqueous solution containing αPD-1 (0.5 mg mL^{-1}). After incubation at 4 °C for 24 h, free antibodies were removed via centrifugation. The obtained CDM-MOF@H/D (α-H/D) nanoparticles were then washed and dispersed in PBS for further use. The loading contents of DEC, HAase, and αPD-1 of the nanodrug were determined to be 0.25%, 7.9%, and 2.8%, respectively.

In vitro release

Human serum albumin labeled with FITC (HAS-FITC) was employed as a model to investigate the release profile of loaded HAase. HAS-FITC and DEC were incorporated into an MOF to produce MOF@-HAS-FITC. Subsequently, αPD-1 was conjugated to MOF@HAS-FITC, yielding αPD-1-MOF@HAS-FITC. This conjugate was dispersed in 15 mL of PBS at pH ~7.4 or ~6.5. The dispersions were subjected to a constant temperature shaker set at 37 °C and 75 rpm. At specific time intervals (1, 2, 4, 6, 8, 12, and 24 h), the dispersion was centrifuged, and 0.5 mL of the supernatant was withdrawn from the system, followed by the addition of 0.5 mL of PBS solution. The concentration of HSA-FITC in the supernatant was measured using a fluorospectrophotometer (F-7100, Hitachi High-Tech Co., Ltd., Tokyo, Japan) at an excitation wavelength of 495 nm and an emission wavelength of 595 nm. DEC was analyzed by high-performance liquid chromatography (HPLC) using an Agilent Technologies 1260 Infinity II (California, USA), equipped with a C18 column (4.6 × 250 mm, 5 μm, Welch). A mixture of acetonitrile and water (60/40, v/v) was used as the mobile phase at a flow rate of 1 mL min^{-1} and a temperature of 40 °C. αPD-1 levels were measured using an ELISA kit (NEOBIOSCIENCE, China). The cumulative release of HAS-FITC, DEC, and αPD-1 from the MOF was quantified based on a standard curve.

In this work, fluorescence resonance energy transfer was utilized to monitor the release behavior of αPD-1 from the MOF surface. Firstly, MOF was labeled with RhoB and coated with NAID-PEG-CDM, followed by the covalent modification with αPD-1 labeled with FITC. The fluorescence emission spectra excited at 480 nm were recorded at different time points after incubation with PBS (pH~6.5).

Cell culture

The mice pancreatic cancer cells (Panc02, Catalog No.CL-0736) were purchased from Wuhan Pricella Biotechnology Co., Ltd (Wuhan, China) and maintained in RPMI-1640 medium supplemented with 10% fetal bovine serum (FBS) and 1% penicillin-streptomycin at 37 °C in a 5% CO_2 humidified incubator. Cell lines were tested negative for mycoplasma contamination by using MycAwayTM-Color one-step Mycoplasma Detection Kit. The luciferase-expressing Panc02-Luc cell line was constructed by Wuhan Pricella Biotechnology Co., Ltd. The CCL5-shRNA-Lentivirus (sequence (5′ to 3′): TTCTCCGAACGTGTCACGT) used to construct stable *CCL5* knockdown Panc02 cells (Panc02/*CCL5* KD) were designed by Suzhou Jima Gene Co., Ltd (Suzhou, China). To construct Panc02 cell lines with stable *CCL5* knockdown, Panc02 cells were seeded in 12-well plates and incubated for 12 h. Then, lentivirus was added to incubate the cells for 48 h. The transfection efficiency was observed under a fluorescence microscope after a fresh medium was added. Puromycin (1 μg mL^{-1}) was added to treat the cells for 24 h to remove non-transfected cells. The remaining cells were collected, seeded in 96-well plates at a cell density of single cell per well, and further cultured for 2 weeks. Panc02 cells expressing only green fluorescent protein (GFP) were collected and expanded to obtain Panc02/*CCL5* KD cells.

TILs and nanodrug-carrying TILs preparation

For the TILs preparation, C57BL/6j mice were anesthetized with sodium pentobarbital (75 mg kg^{-1}) and inoculated subcutaneously with 1×10^6 Panc02 cells suspended in 100 μL sterile PBS. Tumors were harvested once they reached approximately 1 cm in diameter, then minced and digested enzymatically with collagenase IV (Sigma-Aldrich, USA), DNase I (Sigma-Aldrich, USA), and hyaluronidase at 37 °C for 1 h. The resulting cell suspension was filtered through a 70 μm strainer, washed with PBS, and centrifuged at 300 × *g* for 5 min. CD3$^+$ T cells were isolated using anti-CD3 magnetic beads according to the manufacturer's instructions (Miltenyi Biotec). These isolated CD3$^+$ T cells were then cultured in RPMI-1640 medium supplemented with 10% FBS, IL-2 (6000 IU mL^{-1}), IL-12 (2000 IU mL^{-1}), and anti-CD3 antibody (1 μg mL^{-1}) to promote activation and expansion. After 3 days, cells were transferred to larger flasks and maintained at a density of 1×10^6 cells mL^{-1}, with fresh medium, IL-2, and IL-12 added every 3 days to ensure optimal growth conditions. For T cell proliferation, Panc02 cells were seeded into the lower chamber of a Transwell system at a density of 5×10^4 cells per well. After 24 h, TILs were resuspended at a concentration of 5×10^4 cells mL^{-1}, and carboxyfluorescein diacetate succinimidyl ester (CFSE) was added at a final concentration of 2 μM. The suspension was incubated at 37 °C for 10 min. The CFSE labeling reaction was terminated by adding cold PBS. After centrifugation, the labeled TILs were washed twice with cold RPMI medium and transferred to the upper chamber of the Transwell (5.0×10^4 cells mL^{-1}). The TILs were expanded for 14 days and subsequently harvested for downstream applications. To prepare nanodrug-carrying TILs, various concentrations (e.g., 0.1, 0.2, 0.4, 0.6, 0.8 mg mL^{-1}) of the nanodrug were co-incubated with TILs for 24 h, then the cells were centrifuged and collected for further experiments.

In vitro T cell binding

The nanodrug was incubated with cells at pH ~7.4 for 0, 6, 12, or 24 h to allow binding. Subsequently, to assess nanodrug release from T cells, the medium pH was either adjusted to 6.5 or maintained at pH 7.4, and the cells were incubated for an additional 6, 12, or 24 h. For visualizing fluorescence, cells were labeled with Alexa Fluor 647 anti-mouse CD8 antibody and a secondary Alexa Fluor 488 antibody for αPD-1, each for 1 h. Cell nuclei were stained using Hoechst 33342 (Beyotime, China) for 15 min, followed by observation under a confocal laser scanning microscope (CLSM, LSM710, Germany).

ELISA and biochemistry index

To detect HAase activity, the nanodrug or hyaluronidase solution in PBS was allowed to stand for specified intervals (e.g., 12, 24, 48, and 72 h). Subsequently, the samples were analyzed using a hyaluronidase activity enzyme-linked immunosorbent assay (ELISA) kit, following the manufacturer's instructions. To evaluate CCL5 chemokine and cytokine (e.g., TNF-α, IFN-γ, and IL-12p70) expression levels in cell culture supernatants, TILs (1×10^6 mL^{-1}) were co-cultured with tumor cells for 48 h. Following co-culture, the supernatants were collected by centrifugation at 300 × *g* for 5 min. The chemokine and cytokine levels in the supernatants were measured using ELISA kits (according to the manufacturer's instructions) after the samples were harvested and homogenized in radioimmunoprecipitation assay (RIPA) buffer (Beyotime, China) containing protease inhibitors (Beyotime, China). To detect the levels of specific target proteins in tumor tissues, the homogenates were centrifuged at 10,000 × *g* for 15 min at 4 °C, and the resulting supernatants were analyzed using ELISA kits according to the manufacturer's instructions. To detect the TNF-α and IL-6 in the serum, blood samples were collected from mice via retro-orbital bleeding and allowed to clot at room temperature for 30 min. The serum was separated by centrifugation at 2000 × *g* for 10 min. The levels of TNF-α and IL-6 in the serum were measured using ELISA kits according to the manufacturer's instructions. Biochemical parameters were analyzed using an automatic biochemical analyzer (Autobiochemical analyzer, Rayto Chemray 240, China).

TILs killing assay in vitro

For the live cell fluorescence staining, Panc02 cells were seeded at a density of 1×10^5 cells per well in confocal dishes (Nest, China) and cultured for 24 h. After receiving various treatments (PBS, TILs at pH 7.4, TILs-α-H/D at pH 7.4, TILs at pH 6.5, or TILs-α-H/D at pH 6.5), the cells were further cultured for 48 h. TILs (1×10^6 cells per well) were then removed by washing with PBS. The remaining tumor cells were incubated with Calcein-AM (Beyotime, China) for 30 min. Subsequently, the cells were washed three times with PBS and observed using CLSM (LSM710, Germany) to assess live cell staining. For the luciferin-luciferase bioluminescence assay, Panc02-Luc cells (Wuhan Pricella Biotechnology Co., Ltd., China) were seeded in 96-well plates at a density of 1×10^4 and allowed to adhere overnight. TILs (1×10^5 cells per well) were added and co-cultured for 48 h. D-luciferin substrate (Aladdin, China) was then added to the wells at the concentration recommended by the manufacturer. Bioluminescence was measured using a microplate reader (Tecan, Switzerland), with the signal intensity correlating with the number of viable tumor cells.

Animal models

Four-week-old male immunodeficient NOD-Prkdc^{em26Cd52}Il2rg^{em26Cd22}/Nju (NCG) mice were purchased from the GemPharmatech Co., Ltd., 4-week-old male or female C57BL/6j mice were purchased from Guangdong Medical Laboratory Animal Center. All animal procedures were performed in accordance with the Guidelines for Care and Use of Laboratory Animals of Sun Yat-sen University (SYSU) and approved by the Animal Ethics Committee of SYSU. For all surgical procedures, mice were anesthetized with sodium pentobarbital (75 mg kg^{-1}, intraperitoneally), and perioperative pain management was provided in accordance with the requirements of the SYSU Animal Ethics Committee. To develop a subcutaneous tumor model, NCG or C57BL/6j mice were anesthetized, and leg hair was shaved. Panc02 cells (1×10^6) suspended in 100 μL of sterile PBS were subcutaneously injected into the hind legs. For the orthotopic pancreatic tumor model, NCG or C57BL/6j mice were anesthetized, and abdominal hair was removed with depilatory cream. A 1 cm incision was made in the lower left abdomen to expose the pancreas, and Panc02 cells (1×10^6) suspended in 10 μL of sterile PBS were directly injected into the pancreatic tissue. The incision was sutured and disinfected with iodophor. In the establishment of a systemic metastasis model, Panc02-Luc cells (1×10^6) suspended in 100 μL of sterile PBS were injected intravenously via the tail vein. To induce immunosuppression in the C57BL/6j mouse model, cyclophosphamide (Selleck, S1217) was dissolved in 0.9% physiological saline and administered intraperitoneally at a dose of 200 mg kg^{-1} 1 day prior to treatment[50]. At the experimental endpoint or for ex vivo analysis, mice were euthanized by carbon dioxide (CO_2) inhalation followed by cervical dislocation, in compliance with the SYSU Animal Ethics Committee guidelines.

In vivo and ex vivo fluorescence imaging

Following the establishment of the tumor model, mice received an intravenous injection of TILs loaded with nanodrugs (1×10^4 TILs in 100 μL PBS per mouse) via the tail vein. Subsequently, the mice were monitored at predetermined time intervals using an in vivo fluorescence imaging system (FX PRO, Carestream, USA). For ex vivo fluorescence analysis, mice were euthanized 24 h after treatment with nanodrug-loaded TILs. Tumors and principal organs were harvested and imaged separately. Fluorescence intensities were measured and analyzed using semi-quantitative biodistribution techniques within the imaging system.

In vivo antitumor activity

After establishing the tumor model, mice in different groups were injected once with PBS, TILs + α/H/D, and nanodrug-carrying TILs (TILs, TILs-α-H, TILs-α-D, and TILs-α-H/D) through the tail vein. The doses per injection, if applied, were 1×10^6 TILs per mouse. Tumor volume in the subcutaneous tumor model was measured using a caliper and calculated as follows: tumor volume = 0.5 × length × width^2. To measure tumor growth in the orthotopic pancreatic tumor model (Panc02 in C57BL/6j mice), tumor-bearing mice were anesthetized with sodium pentobarbital (75 mg kg^{-1}) and scanned on days 5, 10, and 17 using a 3-T clinical MR scanner (Achieva, Philips Medical Systems, Best, the Netherlands) equipped with a 50-mm small animal coil (Zhongzhi Medical Technologies, Suzhou, China). T_2-weighted images were then acquired. Tumor growth in the systemic metastasis model was evaluated using an in vivo fluorescence imaging system (FX PRO, Carestream, USA).

Histological analysis

Tumor tissues and significant organs were preserved in 4% paraformaldehyde for 2 days at 4 °C and then embedded in paraffin. Representative sections were obtained from a single standardized site for each organ to ensure consistency across samples. Specifically, liver sections were taken from the left lateral lobe, kidney sections were longitudinally prepared from the left kidney, and lung sections were obtained from the largest lobe (left lung). Tissue sections of 2 μm thickness were cut using a microtome (Leica RM2245, Germany) and stained with an H&E staining kit (Solarbio, China) according to the manufacturer's instructions. Stained sections were imaged and analyzed using a Perkin-Elmer Vectra pathology imaging system (USA).

Immunofluorescence staining

Tumor sections were first dewaxed and rehydrated using a series of alcohol solutions. They were then immersed in a heated sodium citrate buffer for antigen retrieval using a microwave oven. The sections were treated with 3% hydrogen peroxide for 15 min, followed by blocking with 5% bovine serum albumin (BSA) for 30 min at room temperature. Overnight incubation with primary antibodies, such as CD8, HA, and CD3, was performed at 4 °C. Following washes with PBST, the sections were exposed to fluorescently tagged secondary antibodies (Abcam, UK) for 1 h. Excess secondary antibodies were washed away with PBST, and the nuclei were stained with DAPI (Beyotime, China) for 5 min. The prepared sections were then examined under a confocal microscope (LSM710, Germany).

Immunohistochemical staining

Tumor sections underwent dewaxing and rehydration through a series of alcohol gradients. These sections were then placed in a heated sodium citrate buffer for antigen retrieval using a microwave. After a 15-min treatment with 3% hydrogen peroxide, the sections were blocked using 5% BSA at room temperature for 30 min, followed by an overnight incubation at 4 °C with antibodies for IFN-γ or granzyme B (Abcam, UK). The sections were washed with PBST and then treated with HRP-conjugated secondary antibodies (Arigo Biolaboratory, China) for 30 min at 37 °C. Staining was completed using a DAB kit (ZSGB-BIO, China), and sections were counterstained with hematoxylin (Solarbio, China) before being examined with a pathology imaging system (Perkin-Elmer Vectra, USA).

Flow cytometric analysis

For proliferation studies, $CD3^+$ TILs were stained with CFSE (Thermo Scientific, USA) before in vitro co-culture experiments with tumor cells. Subsequently, the collected cells were analyzed using flow cytometry assays (NovoCyte 2060R). For evaluating binding efficiency, various concentrations of the nanodrug (e.g., 0.1, 0.2, 0.4, 0.6, 0.8 mg mL^{-1}) were co-incubated with TILs for 12 h, after which the cells were collected and analyzed with flow cytometry assays (NovoCyte 2060R). In the apoptosis study, TILs were co-incubated with similar concentrations of the nanodrug for 12 h. Post incubation, the cells were stained with an apoptosis assay kit (Annexin-V-FITC/PI) and subsequently collected by centrifugation for flow cytometric analysis. For flow cytometry studies, tumor tissues were cut into small pieces, incubated for 30 min in pre-digestion solution, and filtered through a 70 μm cell strainer. Erythrocytes in the resultant cell suspension were eliminated by red cell lysis solution (Solarbio, China). The resulting cells were incubated with TILs-α-RhoB or pre-stained with CellTracker™ CM-DiI dye or surface antibodies, e.g., CD3, CD4, and CD8. The intracellular IFN-γ was stained after fixation with cold 4% paraformaldehyde and permeabilization with 0.1% Triton X-100. Stained cells were analyzed via flow cytometry assays (NovoCyte 2060 R). To assess the exhaustion status of $CD8^+$ and $CD4^+$ TILs, following the above method, cells were isolated and stained with antibodies, e.g., CD3, CD4, CD8, Tim3, and PD-1, and subsequently analyzed by flow cytometry. The corresponding flow cytometry gating strategy is shown in the Supplementary Fig. 23.

Western blot assay

Total proteins were extracted from Panc02 or Panc02 CCL5/KD cells with radioimmunoprecipitation assay (RIPA) buffer and separated by SDS-PAGE gel electrophoresis. Then, the proteins were transferred to polyvinylidene fluoride (PVDF) membranes (Bio-Rad, USA) and then incubated separately with primary antibodies of CCL5 and GAPDH overnight after blocking with 5% non-fat dried milk for 1 h. After washing with TBST for three times, the membranes were incubated with secondary antibodies for 1 h. After washing with TBST for three times, the membranes were incubated with a chemiluminescent substrate for 1 min and visualized on a chemiluminescent system (ProteinSimple FR 0183, USA).

TUNEL analysis

To more accurately quantify the apoptosis of tumor tissues, according to the manufacturer's DAB method (Solarbio, China), the tumor tissue sections underwent several steps, including deparaffinization and rehydration, permeabilization, rinsing, blocking, and TUNEL reaction, and then observed using a pathology imaging system (Perkin-Elmer Vectra, USA).

Statistics and reproducibility

The sample sizes are provided in the respective figure legends and are consistent with common practice in the field. Mice were randomly assigned to the experimental groups. No data were excluded from the analyses. The investigators were not blinded to group allocation during the experiments and outcome assessment. The following experiments were repeated three times independently with similar results: N_2 adsorption, TEM observation, PXRD analysis, SDS-PAGE, CLSM imaging for TIL binding, live cell staining, in vitro TIL infiltration depth assay, CLSM-based visualization of intratumoral TIL distribution, histological analysis, and western blotting. All other experiments were performed at least three times to ensure reproducibility. Data are presented as mean ± SD. Statistical analyses were performed using GraphPad Prism software (Version 10). Differences between the two groups were evaluated using an unpaired two-sided *t*-test. Comparisons among multiple groups were analyzed by unpaired one-way analysis of variance (ANOVA) test. A log-rank (Mantel−Cox) test was conducted to compare the survival curves. Significance levels are denoted as follows: ns no significance; $^*p < 0.05$, $^{**}p < 0.01$, $^{***}p < 0.001$, and $^{****}p < 0.0001$.

Ethical statement

The animal experiments conducted in this study comply with all applicable ethical regulations. All surgical procedures and post-operative care protocols received prior approval from the Institutional Animal Care and Use Committee of Sun Yat-sen University, Guangzhou, China. The assigned approval number of the ethical application of animal experiments is SYSU-IACUC-2023-001684. Animal sex was not considered as a variable in the experimental design, and both males and females were utilized. The approved protocol stipulated that the maximal tumor burden must not exceed a diameter of 2 cm or 10% of the animal's total body weight. No animals in this study surpassed these established limits. All experiments involving animals strictly followed the Animal Management Regulations of China (1988, revised 2017) and the Guideline on the Humane Treatment of Laboratory Animals of China (MOST 2006).

Reporting summary

Further information on research design is available in the Nature Portfolio Reporting Summary linked to this article.

Data availability

The figures of NMR spectra are summarized in Fig. 2a in the article and Supplementary Figs. 2 and 3 in the Supplementary Information and the Source data file. All data supporting the findings of this study are available within the article, Supplementary Information, or Source data file. Source data are provided within this paper. Source data are provided with this paper.

References

1. Mullard, A. FDA approves fourth CAR-T cell therapy. *Nat. Rev. Drug Discov.* **20**, 166 (2021).
2. Ai, K. et al. Optimizing CAR-T cell therapy for solid tumors: current challenges and potential strategies. *J. Hematol. Oncol.* **17**, 105 (2024).
3. Sterner, R. C. & Sterner, R. M. CAR-T cell therapy: current limitations and potential strategies. *Blood Cancer J.* **11**, 69 (2021).
4. Kazemi, M. H. et al. Tumor-infiltrating lymphocytes for treatment of solid tumors: it takes two to tango? *Front. Immunol.* **13**, 1018962 (2022).
5. Wang, S. et al. Perspectives of tumor-infiltrating lymphocyte treatment in solid tumors. *BMC Med.* **19**, 140 (2021).
6. Zhao, Y. et al. Tumor infiltrating lymphocyte (TIL) therapy for solid tumor treatment: progressions and challenges. *Cancers* **14**, 4160 (2022).
7. Hester, R., Mazur, P. K. & McAllister, F. Immunotherapy in pancreatic adenocarcinoma: beyond "copy/paste". *Clin. Cancer Res.* **27**, 6287–6297 (2021).

8. Guo, J., Wang, S. & Gao, Q. An integrated overview of the immunosuppression features in the tumor microenvironment of pancreatic cancer. *Front. Immunol.* **14**, 1258538 (2023).
9. Luo, W., Wen, T. & Qu, X. Tumor immune microenvironment-based therapies in pancreatic ductal adenocarcinoma: time to update the concept. *J. Exp. Clin. Cancer Res.* **43**, 8 (2024).
10. Bear, A. S., Vonderheide, R. H. & O'Hara, M. H. Challenges and opportunities for pancreatic cancer immunotherapy. *Cancer Cell* **38**, 788–802 (2020).
11. Xiao, Z. et al. Dual pH-sensitive nanodrug blocks PD-1 immune checkpoint and uses T cells to deliver NF-kappaB inhibitor for antitumor immunotherapy. *Sci. Adv.* **6**, eaay7785 (2020).
12. Huang, J., Xiao, Z., Lin, M., Zhong, H. & Shuai, X. Metal-organic framework nanoparticles hitchhiking on T cells for protein delivery to boost anticancer immunotherapy. *Nano Today* **54**, 102102 (2024).
13. Tang, L. et al. Enhancing T cell therapy through TCR-signaling-responsive nanoparticle drug delivery. *Nat. Biotechnol.* **36**, 707–716 (2018).
14. Stephan, M. T., Stephan, S. B., Bak, P., Chen, J. & Irvine, D. J. Synapse-directed delivery of immunomodulators using T-cell-conjugated nanoparticles. *Biomaterials* **33**, 5776–5787 (2012).
15. Chen, G. et al. A convenient and versatile amino-acid-boosted biomimetic strategy for the nondestructive encapsulation of biomacromolecules within metal-organic frameworks. *Angew. Chem. Int. Ed.* **58**, 1463–1467 (2019).
16. Chen, X. et al. Non-invasive activation of intratumoural gene editing for improved adoptive T-cell therapy in solid tumours. *Nat. Nanotechnol.* **18**, 933–944 (2023).
17. Dangaj, D. et al. Cooperation between constitutive and inducible chemokines enables T cell engraftment and immune attack in solid tumors. *Cancer Cell* **35**, 885–900 (2019).
18. Xiao, Z. et al. Nanodrug simultaneously regulates stromal extracellular matrix and glucose metabolism for effective immunotherapy against orthotopic pancreatic cancer. *Nano Today* **44**, 101490 (2022).
19. Xiao, Z. et al. Nanodrug removes physical barrier to promote T-cell infiltration for enhanced cancer immunotherapy. *J. Control. Release* **356**, 360–372 (2023).
20. Paijens, S. T., Vledder, A., de Bruyn, M. & Nijman, H. W. Tumor-infiltrating lymphocytes in the immunotherapy era. *Cell. Mol. Immunol.* **18**, 842–859 (2021).
21. Ding, Z. C., Aboelella, N. S., Bryan, L., Shi, H. & Zhou, G. The monocytes that repopulate in mice after cyclophosphamide treatment acquire a neutrophil precursor gene signature and immunosuppressive activity. *Front. Immunol.* **11**, 594540 (2020).
22. Emadi, A., Jones, R. J. & Brodsky, R. A. Cyclophosphamide and cancer: golden anniversary. *Nat. Rev. Clin. Oncol.* **6**, 638–647 (2009).
23. Hu, Z. I. & O'Reilly, E. M. Therapeutic developments in pancreatic cancer. *Nat. Rev. Gastroenterol. Hepatol.* **21**, 7–24 (2024).
24. Zhao, L. & Cao, Y. J. Engineered T cell therapy for cancer in the clinic. *Front. Immunol.* **10**, 2250 (2019).
25. Fernandez-Poma, S. M. et al. Expansion of tumor-infiltrating CD8$^+$ T cells expressing PD-1 improves the efficacy of adoptive T-cell therapy. *Cancer Res.* **77**, 3672–3684 (2017).
26. Mullard, A. FDA approves first tumour-infiltrating lymphocyte (TIL) therapy, bolstering hopes for cell therapies in solid cancers. *Nat. Rev. Drug Discov.* **23**, 238 (2024).
27. Guo, J. et al. Eradicating tumor in a recurrent cervical cancer patient with autologous tumor-infiltrating lymphocytes and a modified lymphodepleting regimen. *J. Immunother. Cancer* **10**, e003887 (2022).
28. Creelan, B. C. et al. Tumor-infiltrating lymphocyte treatment for anti-PD-1-resistant metastatic lung cancer: a phase 1 trial. *Nat. Med.* **27**, 1410–1418 (2021).
29. Reardon, S. First cell therapy for solid tumours heads to the clinic: what it means for cancer treatment. https://doi.org/10.1038/d41586-024-00673-w (2024).
30. Lesch, S. et al. T cells armed with C-X-C chemokine receptor type 6 enhance adoptive cell therapy for pancreatic tumours. *Nat. Biomed. Eng.* **5**, 1246–1260 (2021).
31. Mitchell, M. J. et al. Engineering precision nanoparticles for drug delivery. *Nat. Rev. Drug Discov.* **20**, 101–124 (2021).
32. Goldberg, M. S. Improving cancer immunotherapy through nanotechnology. *Nat. Rev. Cancer* **19**, 587–602 (2019).
33. Milling, L., Zhang, Y. & Irvine, D. J. Delivering safer immunotherapies for cancer. *Adv. Drug Deliv. Rev.* **114**, 79–101 (2017).
34. van Herpen, C. M. et al. Intratumoral rhIL-12 administration in head and neck squamous cell carcinoma patients induces B cell activation. *Int. J. Cancer* **123**, 2354–2361 (2008).
35. Pfreundschuh, M. G. et al. Phase I study of intratumoral application of recombinant human tumor necrosis factor. *Eur. J. Cancer Clin. Oncol.* **25**, 379–388 (1989).
36. Huang, B. et al. Active targeting of chemotherapy to disseminated tumors using nanoparticle-carrying T cells. *Sci. Transl. Med.* **7**, 291ra294 (2015).
37. Reagan-Shaw, S., Nihal, M. & Ahmad, N. Dose translation from animal to human studies revisited. *FASEB J.* **22**, 659–661 (2008).
38. Binnewies, M. et al. Understanding the tumor immune microenvironment (TIME) for effective therapy. *Nat. Med.* **24**, 541–550 (2018).
39. Met, O., Jensen, K. M., Chamberlain, C. A., Donia, M. & Svane, I. M. Principles of adoptive T cell therapy in cancer. *Semin. Immunopathol.* **41**, 49–58 (2019).
40. Levi, S. T. et al. Neoantigen identification and response to adoptive cell transfer in anti-PD-1 naive and experienced patients with metastatic melanoma. *Clin. Cancer Res.* **28**, 3042–3052 (2022).
41. Blass, E. & Ott, P. A. PD-1 inhibition-trouble for subsequent TIL therapy in patients with melanoma? *Clin. Cancer Res.* **28**, 2980–2982 (2022).
42. Zhang, T. et al. Nano-engineered immune cells as "guided missiles" for cancer therapy. *J. Control. Release* **341**, 60–79 (2022).
43. Mitchell, M. J. & King, M. R. Leukocytes as carriers for targeted cancer drug delivery. *Expert. Opin. Drug Deliv.* **12**, 375–392 (2015).
44. Park, W., Chawla, A. & O'Reilly, E. M. Pancreatic cancer: a review. *JAMA* **326**, 851–862 (2021).
45. Springfeld, C. et al. Neoadjuvant therapy for pancreatic cancer. *Nat. Rev. Clin. Oncol.* **20**, 318–337 (2023).
46. Ullenhag, G. J. et al. Adoptive T-cell therapy for malignant melanoma patients with TILs obtained by ultrasound-guided needle biopsy. *Cancer Immunol. Immunother.* **61**, 725–732 (2012).
47. Schietinger, A. et al. Tumor-specific T cell dysfunction is a dynamic antigen-driven differentiation program initiated early during tumorigenesis. *Immunity* **45**, 389–401 (2016).
48. Trehan, R. et al. SPP1 + macrophages cause exhaustion of tumor-specific T cells in liver metastases. *Nat. Commun.* **16**, 4242 (2025).
49. Takeuchi, Y. et al. Exhaustion, rather than lack of infiltration and persistence, of CAR-T cells hampers the efficacy of CAR-T therapy in an orthotopic PDAC xenograft model. *Biomed. Pharmacother.* **170**, 116052 (2024).
50. Tian, H. et al. Complement C1q binding protein regulates T cells' mitochondrial fitness to affect their survival, proliferation, and anti-tumor immune function. *Cancer Sci.* **113**, 875–890 (2022).

Acknowledgements

We thank the members of the Shuai laboratories for helpful discussions and technical assistance. This study was supported by the National Key R&D Program of China (2023YFF0724200, X.S., and Z.X.), National Natural Science Foundation of China (82102194, Z.X., 32301195, S.D.), the Science and Technology Projects of Guangzhou (2023A03J0215, X.S.) and GuangDong Basic and Applied Basic Research Foundation (2023A1515140079, S.D., 2024A1515012500, S.D.).

Author contributions

Z.X. and X.S. conceived and designed the nanodrug and experimental program. Z.G., Z.X., J.H., S.D. (Shuting Duan), M.L., S.D. (Shaohui Deng), S.H., and J.W. performed the experiments and data analysis. The manuscript was written by Z.X., Z.G., and J.H. and finally approved by Z.X. All authors contributed feedback on the final manuscript.

Competing interests

The authors declare no competing interests.

Additional information

Supplementary information The online version contains supplementary material available at https://doi.org/10.1038/s41467-025-67254-x.

Correspondence and requests for materials should be addressed to Ziqi Gan, Xintao Shuai or Zecong Xiao.

Peer review information *Nature Communications* thanks Hongbin Ji, Daniel Öhlund and the other anonymous reviewer(s) for their contribution to the peer review of this work. A peer review file is available.

Reprints and permissions information is available at http://www.nature.com/reprints

Publisher's note Springer Nature remains neutral with regard to jurisdictional claims in published maps and institutional affiliations.

Open Access This article is licensed under a Creative Commons Attribution-NonCommercial-NoDerivatives 4.0 International License, which permits any non-commercial use, sharing, distribution and reproduction in any medium or format, as long as you give appropriate credit to the original author(s) and the source, provide a link to the Creative Commons licence, and indicate if you modified the licensed material. You do not have permission under this licence to share adapted material derived from this article or parts of it. The images or other third party material in this article are included in the article's Creative Commons licence, unless indicated otherwise in a credit line to the material. If material is not included in the article's Creative Commons licence and your intended use is not permitted by statutory regulation or exceeds the permitted use, you will need to obtain permission directly from the copyright holder. To view a copy of this licence, visit http://creativecommons.org/licenses/by-nc-nd/4.0/.

© The Author(s) 2025